SPECIAL
Spontaneous Imbalance
COLLECTION

Global Gravity Wave Variances from *Aura* MLS: Characteristics and Interpretation

DONG L. WU

Jet Propulsion Laboratory, California Institute of Technology, Pasadena, California

STEPHEN D. ECKERMANN

Space Science Division, Naval Research Laboratory, Washington, D.C.

(Manuscript received 2 April 2007, in final form 11 March 2008)

ABSTRACT

The gravity wave (GW)–resolving capabilities of 118-GHz saturated thermal radiances acquired throughout the stratosphere by the Microwave Limb Sounder (MLS) on the *Aura* satellite are investigated and initial results presented. Because the saturated (optically thick) radiances resolve GW perturbations from a given altitude at different horizontal locations, variances are evaluated at 12 pressure altitudes between ~21 and 51 km using the 40 saturated radiances found at the bottom of each limb scan. Forward modeling simulations show that these variances are controlled mostly by GWs with vertical wavelengths $\lambda_z > 5$ km and horizontal along-track wavelengths of $\lambda_y \sim 100$–200 km. The tilted cigar-shaped three-dimensional weighting functions yield highly selective responses to GWs of high intrinsic frequency that propagate toward the instrument. The latter property is used to infer the net meridional component of GW propagation by differencing the variances acquired from ascending (A) and descending (D) orbits. Because of improved vertical resolution and sensitivity, *Aura* MLS GW variances are ~5–8 times larger than those from the *Upper Atmosphere Research Satellite* (*UARS*) MLS. Like *UARS* MLS variances, monthly-mean *Aura* MLS variances in January and July 2005 are enhanced when local background wind speeds are large, due largely to GW visibility effects. Zonal asymmetries in variance maps reveal enhanced GW activity at high latitudes due to forcing by flow over major mountain ranges and at tropical and subtropical latitudes due to enhanced deep convective generation as inferred from contemporaneous MLS cloud-ice data. At 21–28-km altitude (heights not measured by the UARS MLS), GW variance in the tropics is systematically enhanced and shows clear variations with the phase of the quasi-biennial oscillation, in general agreement with GW temperature variances derived from radiosonde, rocketsonde, and limb-scan vertical profiles. GW-induced temperature variances at ~44-km altitude derived from operational global analysis fields of the ECMWF Integrated Forecast System in August 2006 reveal latitudinal bands of enhanced GW variance and preferred GW meridional propagation directions that are similar to those inferred from the MLS variances, highlighting the potential of MLS GW data for validating the stratospheric GWs simulated and/or parameterized in global models.

1. Introduction

Gravity waves (GWs) play a key role in the global meteorology, climate, chemistry, and microphysics of the stratosphere and mesosphere (Fritts and Alexander 2003). Because finite computational resources force global climate–chemistry and weather prediction models to run at spatial resolutions that do not adequately resolve GW dynamics, these important GW-induced effects must be parameterized (e.g., McLandress 1998; Kim et al. 2003). Arguably the greatest weakness in current GW parameterizations is their poorly constrained specifications of lower atmospheric sources (see, e.g., McLandress and Scinocca 2005). Although it is recognized that GWs can be excited by flow across mountains, convection, and imbalance/instability within rapidly evolving baroclinic jet/frontal systems (e.g., Fritts et al. 2006), the relative contributions of these sources to the GW spectrum encountered in the middle atmosphere remains highly uncertain, particularly with respect to GWs radiated from jet imbalance (see, e.g., section 7h of Kim et al. 2003).

Direct measurements of GWs by advanced satellite

Corresponding author address: Dong Wu, M/S 183-701, Jet Propulsion Laboratory, California Institute of Technology, 4800 Oak Grove Drive, Pasadena, CA 91109.
E-mail: dong.l.wu@jpl.nasa.gov

DOI: 10.1175/2008JAS2489.1

remote sensors can reduce some of these uncertainties (Wu et al. 2006a). One of the first satellite instruments to provide global measurements of stratospheric GWs was the Microwave Limb Sounder (MLS) on the *Upper Atmosphere Research Satellite* (*UARS*; Wu and Waters 1996, 1997). Those measurements provided initial insights into some of the major orographic and deep convective sources of GWs for the middle atmosphere (e.g., McLandress et al. 2000; Jiang et al. 2002, 2004a,b, 2005, 2006). A new MLS instrument on the Earth Observing System (EOS) *Aura* satellite started acquiring data in July 2004. In this study we extend the analysis of GWs using saturated thermal stratospheric radiances from the UARS MLS to the new radiances now being acquired by the *Aura* MLS. The new instrument was designed to measure atmospheric composition with emphasis on the upper troposphere and lower stratosphere (UTLS). One of the seven *Aura* MLS radiometers measures thermal O_2 emission features near 118 GHz with sensitivity, vertical resolution, and spectral coverage that are all much improved over the UARS MLS 63-GHz measurements acquired during 1991–97. Thus, the *Aura* MLS 118-GHz radiances are more sensitive to GWs than the earlier *UARS* MLS 63-GHz measurements.

The stratospheric GWs observed by the MLS differ from those observed by other satellite instruments in at least two important ways. First, the MLS GW product is not derived from the retrieved temperature, as is the case for other limb sounders such as LIMS (Limb Infrared Monitor of the Stratosphere; Fetzer and Gille 1994), CRISTA (Cryogenic Infrared Spectrometers and Telescopes for the Atmosphere; Preusse et al. 2002), GPS/MET occultation (meteorological applications of the Global Positioning System; Tsuda et al. 2000), and SABER (Sounding of the Atmosphere using Broadband Emission Radiometry; Preusse et al. 2006). These techniques deduce atmospheric pressure and/or temperature from optically thin radiances and can measure GW-induced temperature perturbations with slightly better vertical resolution but relatively poorer horizontal resolution than MLS. Thus, the resolved GW-induced temperature variances from these instruments correspond to different portions of the three-dimensional (3D) GW wavenumber spectrum than those based on saturated radiances (Wu et al. 2006a). Second, the MLS radiance responses to GW-induced temperature perturbations are very sensitive to the wave's horizontal propagation direction, unlike GW data from nadir sounders, such as the Advanced Microwave Sounding Unit A (AMSU-A; Wu 2004) and the Atmospheric Infrared Sounder (AIRS; Alexander and Barnet 2007), and from other limb sounders, such as LIMS, CRISTA, and SABER. Because MLS has a very shallow viewing angle (3°–8° above the local horizon) and a narrow field of view (FOV), its saturated radiances have 3D weighting functions (WFs) that are tilted up from the horizon with an aspect ratio of ~1:10 for the vertical to horizontal length scales. When tilted GW phase structures coalign with these tilted WFs, they produce a strong radiance perturbation signal. As a result, the GW-induced radiance variance observed by MLS can differ significantly, depending on the viewing direction with respect to horizontal GW propagation. Thus, variance differences for the same GWs observed by MLS from different viewing angles can be used to infer anisotropies in GW horizontal propagation directions (Jiang and Wu 2001). Such a viewing-dependent difference in response is clearly evident after sorting monthly-mean variances from ascending (i.e., satellite latitude increasing with time) and descending (i.e., satellite latitude decreasing with time) orbits (Wu and Waters 1997).

The paper is organized as follows: Section 2 describes the *Aura* MLS instrument, focusing on the 118-GHz thermal channels that resolve GW perturbations in saturated radiance measurements. Section 3 outlines our variance calculations and the sensitivity of these radiance variances to GWs of different wavelengths and horizontal propagation directions. Section 4 presents these variances as a function of altitude, season, and geographical location as a means of inferring information on stratospheric GW amplitudes, horizontal propagation directions, and source characteristics. In section 5, MLS GW variances are cross-correlated at 45-km altitude in August 2006 with small-scale GW-induced temperature oscillations explicitly resolved in high-resolution global analysis fields issued by the European Centre for Medium-Range Weather Forecasts (ECMWF) Integrated Forecast System (IFS). Section 6 summarizes major results from this study and briefly discusses areas for future work.

2. The MLS Experiment on *Aura*

The *Aura* MLS scans the atmospheric limb continuously. Each scan, also called a major frame (MAF), takes 24.7 s, covers tangent heights h_t ranging from the surface ($h_t = 0$ km) to $h_t \approx 92$ km (Waters et al. 2006), and is separated horizontally from adjacent scans by ~165 km. Each MAF is further divided into 148 minor frames (MIFs) with ~120 MIFs devoted to atmospheric measurements.

We focus here on thermal radiances from the 25 channels centered on the strong 118-GHz O_2 line (channel 13) and its various wing line emissions that are

TABLE 1. *Aura* MLS 118-GHz radiance noise in normal operation.

MLS channels	Saturation height (km)	Instrument $\sigma_e^2(n)$[a] (K^2)	Minimum detectable GW variance ($\times 10^{-3}$ K^2)			
			Maps[b]		Zonal mean[c]	
			Monthly	5 day	Monthly	Daily
1 (25)	21.7	0.061	2.3	5.6	0.38	2.3
2 (24)	23.0	0.065	2.4	5.9	0.4	2.4
3 (23)	24.3	0.065	2.4	5.9	0.4	2.4
4 (22)	25.6	0.095	3.5	8.6	0.59	3.5
5 (21)	27.3	0.094	3.5	8.5	0.58	3.5
6 (20)	29.1	0.098	3.7	8.9	0.61	3.7
7 (19)	31.9	0.12	4.6	11	0.77	4.6
8 (18)	34.3	0.19	7.0	17	1.2	7.0
9 (17)	37.0	0.24	8.9	22	1.5	8.9
10 (16)	40.1	0.36	13	33	2.2	13
11 (15)	44.1	0.46	17	42	2.9	17
12 (14)	50.8	0.69	26	63	4.3	26

[a] This noise variance is approximately one-half of the single-channel noise variance as a result of combining the symmetric channel pairs.

[b] A grid box of 5° × 10° (latitude–longitude) is used in this averaging.

[c] These zonal means have a 5° latitude bin.

distributed symmetrically about the center line and that saturate at progressively lower heights in the atmosphere (see Table 1). In the normal operation mode (Waters et al. 2006), each of these *Aura* MLS channels yields more than 40 saturated radiance measurements at the bottom of each scan that can be used for GW analysis, compared to only six saturated measurements in the *UARS* MLS 63-GHz thermal radiance channels. According to radiative transfer theory, the saturated microwave radiance is a direct measurement of blackbody emission of atmospheric air at a particular altitude layer defined by the temperature WF. Fluctuations in the saturated radiances occur because of air temperature fluctuations within that layer, and one can derive the GW-induced temperature variance from these radiance fluctuations. The increased number of saturated radiance measurements from *Aura* MLS means that the GW variance can be estimated more precisely using data from a single scan.

Because GWs have 3D phase structures that depend on phase speed, propagation direction, and the background environment, the MLS viewing geometry, which affects the orientation and shape of the WFs, is important for understanding its sensitivity to various types of GWs. The *Aura* MLS 118-GHz radiance channels have an angular FOV with a full-width half-maximum (FWHM) of ~0.113°, corresponding to a vertical width of ~4.9 km (Cofield and Stek 2006) at the volume where the radiance is saturated, which is located ~2500 km from the spacecraft. The *UARS* MLS 63-GHz FOV is ~0.206°, or ~9.6-km vertical width at the limb (Jarnot et al. 1996; Wu and Waters 1996), much broader than that of the *Aura* MLS. Another important difference for GW detection is that the *UARS* MLS observed at 90° to the spacecraft motion, whereas *Aura* MLS observes along the direction of spacecraft motion. The *Aura* MLS cross-track FOV at 118 GHz is ~0.23° (Cofield and Stek 2006), or ~10 km at the limb. Because of the forward-viewing *Aura* MLS geometry, this cross-track width of the 3D WF has a much smaller influence on GW detection compared to the much longer WF widths along track. Therefore, in this paper we focus only on how the two-dimensional (2D) WF cross-sections along the orbit plane affect GW detection. Unlike UARS, *Aura* does not make periodic yaw maneuvers that interrupt sampling patterns, and so the forward-viewing *Aura* MLS measurements cover latitudes between 82°S and 82°N every day.

Aura MLS can resolve GW perturbations down to UTLS altitudes using radiances from other frequency channels located well away from the 118-GHz O_2 line. Because most GWs are generated in the troposphere, these new UTLS GW observations are especially valuable in pushing the MLS GW measurements down closer to source regions. MLS GW observations in the troposphere rely primarily on the four wideband channels at 115.2, 117.0, 120.5, and 122.0 GHz. However, the 115.2- and 122.0-GHz radiances can be contaminated by cloud scattering and the 117.0- and 120.5-GHz channels have fewer than 40 useful saturated radiance measurements. Because MLS GW variances are sensitive to the number of radiance measurements used in the calculation (see, e.g., Fig. 3 of Jiang et al. 2002), here we require that each channel must have 40 saturated radi-

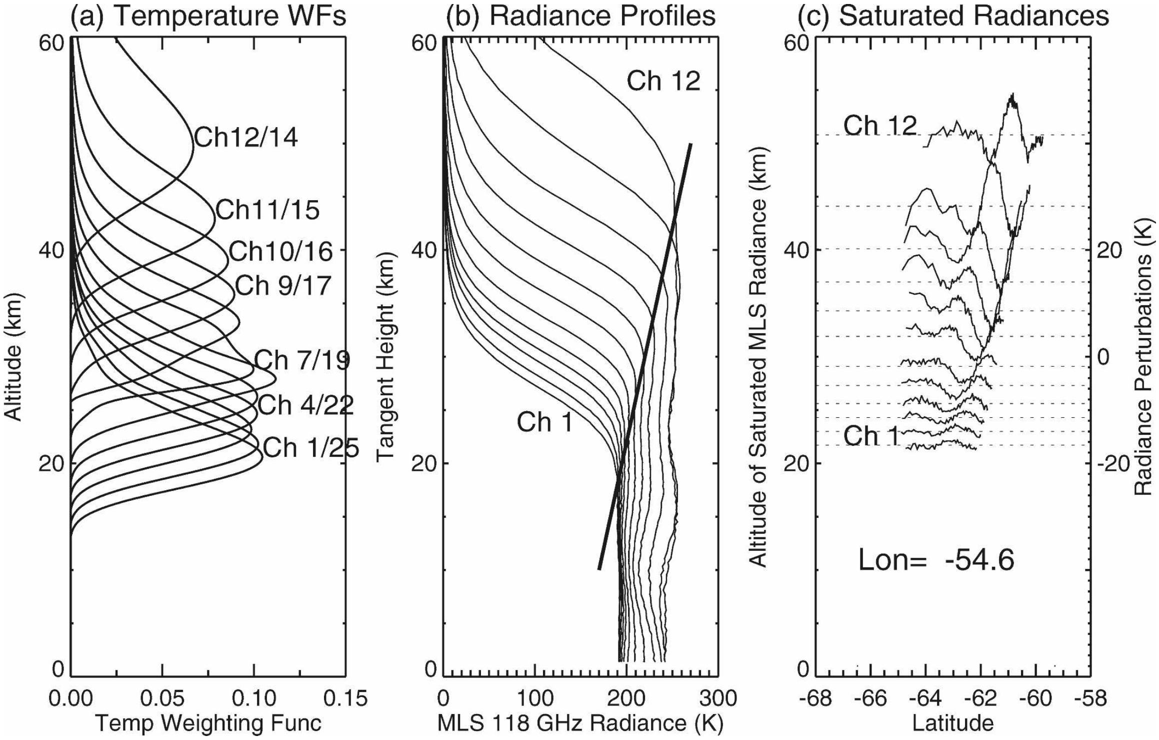

FIG. 1. (a) MLS horizontally integrated temperature weighting functions, (b) limb radiance profiles, and (c) saturated radiance perturbations from a scan over northern tip of Antarctic Peninsula (63°S, 55°W) at 0402:48 UTC 2 Sep 2004. The weighting functions represent the derivatives of the saturated radiance with respect to atmospheric temperature (Read et al. 2006) and provide 12 distinct layers from the 25 channels (excluding channel 13). The straight line in (b) separates (roughly) saturated and unsaturated radiances. The perturbations in (c) are perturbations of the saturated radiance in (b) at low tangent heights, except that they are plotted as a function of latitude (see text). The latitude of these radiances reflects the actual location where saturation takes place. Note that the phase of perturbations is shifted with respect to altitude, tilted toward the MLS. The arrow in (c) indicates the *Aura* flight direction (the same as the MLS viewing direction).

ance measurements in a given scan, which limits our study to the 25 channels near 118 GHz and excludes the wideband measurements. As shown in Fig. 1a (see also Table 1), the lowest temperature WF peak from these 25 channels occurs at a pressure height of ~21.7 km.

Figure 1b shows these various channel radiances from an MLS scan located near the northern tip of the Antarctic Peninsula at 0402:48 UTC 2 September 2004. Large-amplitude oscillations are evident in the saturated portions of the radiance profiles measured at low h_t: the thick solid line in Fig. 1b roughly demarks the unsaturated upper-level radiances from the saturated lower-level radiances for each channel. When a limb radiance saturates, the altitude of its temperature WF (see Fig. 1a) remains roughly constant even though the instrument is scanning vertically. In this case, as depicted in Fig. 2a, vertical scanning then leads to horizontal displacement of the atmospheric volumes, yielding the saturated limb radiances. We fit and then remove a linear trend (due to a slight change in viewing angle) in the saturated radiances to isolate perturbations. The perturbations in saturated radiances from a given channel arise from horizontal temperature variations at the channel's saturation altitude (see Fig. 2a). Figure 1c plots the perturbations extracted from the saturated radiances from channels 1–12 in Fig. 1b, mapped (based on the saturation altitude and viewing tangent height) to the precise latitude and longitude of the volume along the line-of-sight (LOS) ray to the altitude where the channel is saturated (Fig. 1a): the variation of MLS LOS with latitude is shown in Fig. 2b. This remapping procedure yields variations as a function of latitude (Fig. 1c) and longitude (not shown) at each channel's saturation pressure altitude, which ranges from ~22 km for channels 1 and 25 to ~51 km for channels 12 and 14 (see Table 1), assuming a constant scale height of 6.95 km. The along-track distances spanned by the saturated limb radiances in a given MAF vary between 1° and 4° (or 100–400 km) during normal operation (see Fig. 1c), which is determined by the satellite motion (~7 km s^{-1}), the MLS scan rate, and the number of saturated radiance measurements in

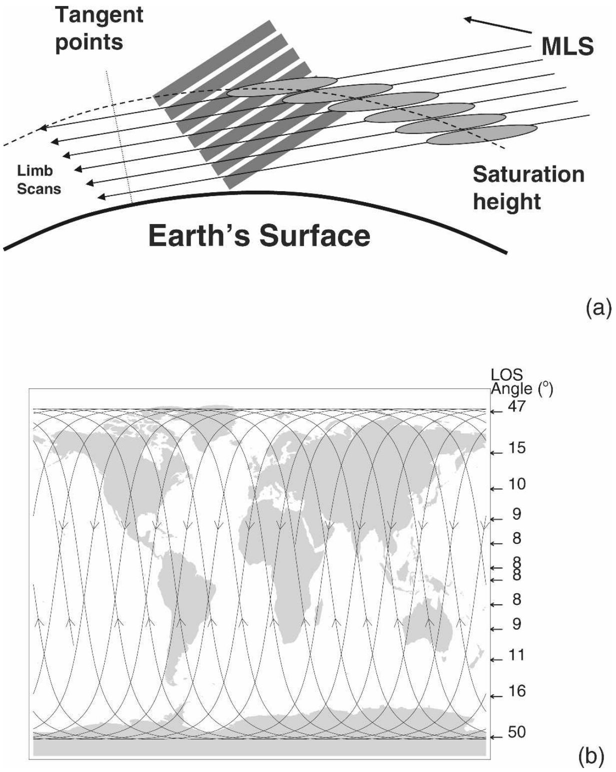

FIG. 2. (a) A schematic diagram of an MLS scan, showing the 2D cross sections through the 3D temperature weighting functions (gray-shaded cigarlike volume) of saturated limb radiances with respect to wave propagation structures (dark gray linear phase lines). The *Aura* MLS flight direction is indicated by the short thick arrow. As the MLS scans vertically, the peak altitudes of these WFs of the saturated radiances change very little, but the WFs are displaced horizontally as shown, giving unique sensitivity to the horizontal structure of gravity waves propagating in the saturation layer (dotted line). (b) An example of the *Aura* MLS sampling track with ascending and descending orbits indicated by up and down arrows. The LOS viewing angles with respect to the meridian are indicated on the right as a function of latitude.

each channel (see Fig. 1b). For the GW event isolated in Fig. 1c, the wave-induced radiance amplitude exceeds 10 K in channels 10–12, has an along-track wavelength of ~200 km, and shows linear phase tilting with altitude, the "fingerprint" of a gravity wave oscillation.

To compute GW-induced variances, we use the 40 saturated radiances observed by a single channel at the bottom of each scan during normal operation (Fig. 1b) and estimate the radiance variance for this channel in this scan. Thus, each MLS GW variance is uniquely associated with a radiance channel, which in turn is identified with a characteristic pressure altitude, defined here as the peak of the vertical WF for that channel's saturated radiances (Fig. 1a). The GW variance derived from these data is fundamentally different from variances deduced from the retrieved temperature, for which the retrieval algorithm has combined unsaturated radiances from multiple channels in a least squares sense to yield a temperature profile that varies vertically, not horizontally. In the radiance variance analysis used here, although some higher-altitude channels may contain more than 40 saturated radiances, it is important to apply a uniform truncation of 40 points to all channel data since the GW variances are very sensitive the truncation length used (e.g., McLandress et al. 2000; Jiang et al. 2002). The 40-point (pt) cutoff corresponds to a horizontal truncation length of ~140 km along track, and therefore GWs with along-track horizontal wavelengths longer than this do not contribute significantly to these variances.

3. Variance and sensitivity analyses

a. GW variance calculation

The GW variance calculation is carried out as follows: The 40 saturated radiances are first fitted with a linear function. Then, the residuals from the fit are combined for the symmetric channel pairs (e.g., channels 1 and 25: see Table 1) because they have similar WFs and the signal-to-noise ratio (SNR) of the resulting variance is improved by a factor of 2 compared to single-channel variances. The resulting radiance variance (hereafter called the 40-pt variance) contains contributions from instrument noise (σ_e^2) and GW-induced variance (σ_{GW}^2); that is,

$$\sigma^2(n) = \sigma_{\mathrm{GW}}^2(n) + \sigma_e^2(n), \tag{1}$$

where n denotes the channel number from 1(25) to 12(14). As shown in Fig. 1c, each scan produces 12 GW variance estimates, each of which has a unique pressure altitude determined by that channel's WF peak.

We can derive the GW variance using Eq. (1) if the radiance variance and noise can both be estimated accurately: that is, $\sigma_{\mathrm{GW}}^2(n) = \sigma^2(n) - \sigma_e^2(n)$. For the *Aura* MLS, the noise variance σ_e^2 can be determined with high precision using radiance measurements at high tangent heights where there is no atmospheric signal. However, as described by Wu and Waters (1997) for the *UARS* MLS, the σ^2 estimate is subject to statistically random noise that dominates the final uncertainty of the σ_{GW}^2 estimate. Uncertainties in the measured variance $\hat{\sigma}^2$ depend on the noise variance σ_e^2 in the case where $\sigma_{\mathrm{GW}}^2 \ll \sigma_e^2$. Wu and Waters (1997) showed that the estimated variance $\hat{\sigma}^2$ has an uncertainty of $\sqrt{2/(M-2)}\sigma_e^2$ for an M-pt variance estimation, which yields $\sim 0.23\sigma_e^2$ for $M = 40$, a value sometimes too large to permit statistically significant σ_{GW}^2 estimates. Thus, further averaging is required to reduce uncertainties in the final σ_{GW}^2 estimate.

One approach to improving the σ^2_{GW} statistics is to average the variance measurements over a period of time or over a large geographical region. The variance uncertainty will be reduced to $0.23\sigma_e^2/\sqrt{J}$ if J is the number of independent variance measurements that are averaged. A trade-off between spatial and temporal averaging needs to be made, depending on the GW problems of interest. Averaging over a long period of time helps to detect weak GW variances over an isolated geographical region (e.g., Jiang et al. 2004a) but removes information on short-term variability. On the other hand, variances averaged over a large geographical domain (e.g., zonal means) can yield statistically significant GW information on daily time scales, but with the loss of regional information (e.g., zonal asymmetries). If GWs occur persistently or frequently over a given geographical region, we typically choose to average the variances over a long period of time (say, 1 month) within a small region, such as a 5° × 10° latitude–longitude box. Within a 5° × 10° grid box, the *Aura* MLS typically produces about six profiles every 5 days from just the ascending orbits alone, which would improve the minimum detectable variance of channel 1(25) to 5.6×10^{-3} K^2. For a monthly mean, this lower limit can be reduced still further to 2.3×10^{-3} K^2. Estimated noise variances σ_e^2 and statistical uncertainties for σ^2_{GW} under various averaging scenarios are listed in Table 1 for all 12 MLS channel pairs. In section 4 we analyze GW variances σ^2_{GW} derived from some of these different averaging scenarios.

In addition to the variance averaging, the truncation length M used in the variance calculation can also affect the value of minimum detectable GW variance. Because stratospheric GWs show larger temperature variances at long horizontal wavelengths (e.g., Bacmeister et al. 1996; Koshyk and Hamilton 2001; Wu 2001), a longer truncation length should yield larger GW variance values. In the MLS case, the truncation length is limited by the number of saturated radiances within each scan, except for special limb-tracking operations in which saturated data sequences can span thousands of kilometers. *UARS* MLS limb-tracking observations show that GW variances increase exponentially with horizontal scales between 100 and 1000 km (McLandress et al. 2000; Wu 2001; Jiang et al. 2002).

b. MLS GW visibility function

As with other GW-resolving satellite sensors (Alexander 1998; McLandress et al. 2000; Preusse et al. 2002; Jiang et al. 2004a; Wu 2004; Eckermann and Wu 2006), interpreting *Aura* MLS variances requires a comprehensive understanding of the instrument's sensitivity to GWs of different wavelengths and propagation directions. Specifying this so-called MLS GW visibility function in turn requires knowledge of the 3D temperature WFs of the saturated limb radiance. As discussed in section 2, because *Aura* MLS scans within the orbital plane in the forward direction, the most critical part of the WF for GW detection is the 2D cross section in the along-track (along-scan) direction, also known as the orbital plane. Figure 2a schematically depicts a series of these 2D WF cross sections: as with *UARS* MLS, the width in the cross-scan direction is narrow and is determined mainly by the ~0.23° horizontal FOV of the antenna. In the orbital plane, MLS WFs appear as narrow, cigar-shaped volumes that are tilted ~3°–8° from the local horizon at their saturation altitude. As with saturated *UARS* MLS radiances, this tilting is a net effect of the MLS viewing angle, antenna spreading at the saturation altitude, and the width and shape of the vertical temperature WF (Wu and Waters 1997; McLandress et al. 2000; Jiang et al. 2004a). The MLS sensitivity to GWs of short vertical wavelengths is determined primarily by the FOV's vertical FWHM, which is 4.9 km, even though the long dimension of the cigar-shaped WF can stretch to over 10 km vertically (see Fig. 2a). More accurate radiative transfer calculations show that the cigar-shaped volume approximates the 2D WF cross section quite well, except near the bottom of the WFs where strong absorption breaks the symmetry about the LOS axis slightly and skews the WF shapes (Wu and Waters 1997).

We model the 2D MLS GW visibility functions in the along-scan (y–z) plane by convolving the 2D instrument WFs through an infinite plane temperature wave of 1-K amplitude and with given values of vertical (λ_z) and along-track (λ_y) wavelength. The signs of λ_z and λ_y are chosen such that the GW energy propagates upward and toward the instrument. Microwave absorption is approximated using a Lorentz line-shape approximation (e.g., Eckermann and Wu 2006) and peaks at a pressure height of ~30 km, roughly approximating saturated radiances from channel 6(20). The resulting 2D WFs are computed using realistic microwave radiative transfer, antenna spreading, and spherical geometry (Cofield and Stek 2006) on a 2D grid of 100-m vertical and 1000-m horizontal resolution. From the simulated (forward modeled) radiance perturbations, we compute the 40-pt radiance variances using the same method outlined in section 3a and repeat the simulation for the full range of possible λ_y and λ_z wavelength pairs.

The calculated 2D visibility function for MLS 40-pt variances is shown in Fig. 3a. The peak variance sensitivity occurs at $\lambda_y \approx 130$ km and $\lambda_z \approx 14$ km, where the variance calculated from the simulated radiances

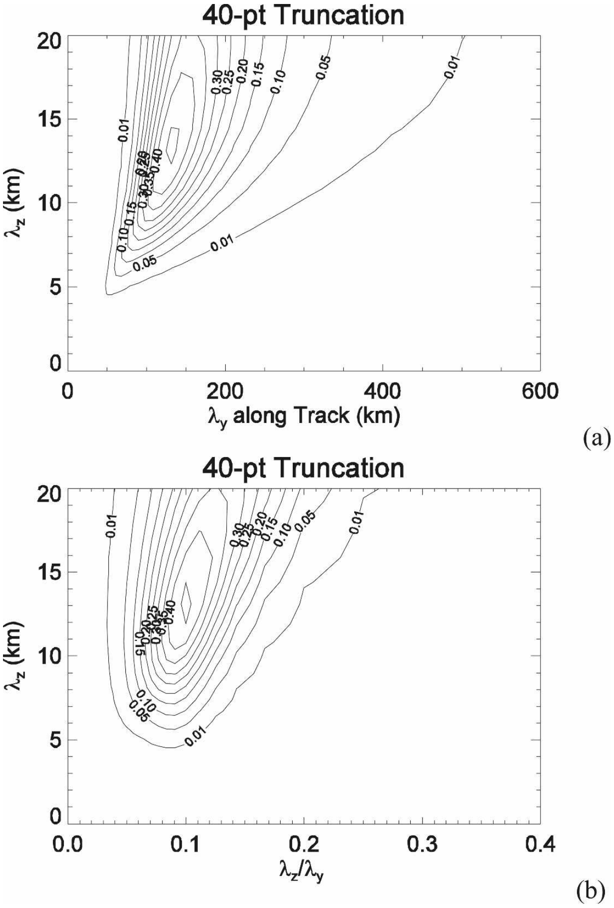

FIG. 3. MLS GW visibility function for the 40-pt variance calculation (a) as a function of along-track wavelength λ_y and vertical wavelength λ_z and (b) as a function of λ_z/λ_y ratio and λ_z. Contour labels are radiance variances (K^2) for an input GW peak amplitude of 1 K (variance of 0.5 K^2). See text for further details.

(brightness temperatures) is 0.47 K^2, representing ~94% "visibility" to the input GW's actual temperature variance of 0.5 K^2. This is a case where the GW propagates upward and toward MLS and its phase lines, tilted off the horizontal at an angle $\phi = \tan^{-1}(\lambda_z/\lambda_y)$ ~6°, are nearly parallel to the instrument's similarly tilted 2D WF in Fig. 2a, so there is essentially no smearing of wave phase along the LOS direction. When this same GW propagates away from the instrument (λ_y changes sign), the variance response becomes negligible ($<6 \times 10^{-3}$ K^2) because phases are no longer coaligned with the 2D WFs and appreciable LOS smearing occurs. This directional sensitivity is now studied further.

Figure 3a shows that *Aura* MLS sensitivity to along-track wavelengths tapers off at $\lambda_y < \sim 100$ km and $\lambda_y > \sim 170$ km. The diminishing sensitivity at short λ_y is due to the along-track smearing by the antenna pattern, satellite motion, and radiative transfer, whereas at long λ_y it is due to the 40-pt truncation. The smearing effects of radiative transfer and MLS FOV also limit the sensitivity to waves of small λ_z and λ_y = 100–200 km.

Figure 3b indicates that the *Aura* MLS has optimal sensitivity to GWs with λ_z/λ_y aspect ratios of ~0.1 that yield a tilt angle ϕ similar to those of the 2D WFs. From the hydrostatic nonrotating GW dispersion relation, this implies peak sensitivity to GWs with intrinsic frequencies $\omega = (\lambda_z/\lambda_y)N \approx 0.1N$, where N is the background Brunt–Väisälä (BV) frequency, or with intrinsic wave periods of ~1 h, given typical stratospheric BV periods of ~5 min. Thus, these 40-pt variances are most sensitive to medium-scale GWs of relatively high intrinsic frequency. The variances have poor sensitivity to low-frequency inertia GWs, which, from the dispersion relation, have λ_z/λ_y ratios of ~0.01–0.001. In other words, inertia GWs surviving MLS WF filtering will have long λ_y values that will not survive the 40-pt horizontal truncation.

c. *Sensitivity to horizontal propagation*

The highly directional tilting of the *UARS* MLS 2D WFs yielded a complex 3D in-orbit sensitivity to GWs that is depicted schematically in Fig. 2 of Jiang et al. (2004a) and was modeled in detail by McLandress et al. (2000) and Jiang et al. (2004a) to aid comparisons between model results and observations. As depicted in Fig. 2a, the 2D tilted *Aura* MLS WFs also yield a directional sensitivity in response to GWs, although it is different from the *UARS* MLS in terms of viewing direction, channel specifics, and antenna widths.

The *Aura* satellite is in a 98.2°-inclination orbit, and the onboard MLS views the atmosphere directly ahead of the satellite (i.e., in the direction of the satellite velocity vector). This yields an MLS LOS (y) axis directed 8.2° from the meridional plane at latitudes near the equator (Fig. 2b). As we have noted in section 3b and Fig. 3, upward-propagating GWs with $\lambda_z > 10$ km and $\lambda_z/\lambda_y \approx 0.1$ are well detected by MLS when they propagate toward the instrument, but yield little or no signal when propagating away from the instrument. As a result, at low latitudes the GW variances from the ascending and descending orbits—$\sigma_A^2(n)$ and $\sigma_D^2(n)$, respectively—are sensitive mostly to GWs propagating southward $\sigma_S^2(n)$ and northward $\sigma_N^2(n)$, respectively, but with a small eastward/westward component $\sigma_{EW}^2(n)$ in both cases. Mathematically, we may express this as

$$\sigma_A^2(n) = \sigma_S^2(n) + \sigma_{EW}^2(n), \tag{2a}$$

$$\sigma_D^2(n) = \sigma_N^2(n) + \sigma_{EW}^2(n), \tag{2b}$$

where n is channel number. In Eqs. (2a) and (2b) we assume that $\sigma_A^2(n)$ and $\sigma_D^2(n)$ are sufficiently averaged as to be not biased by any transient large-amplitude GW event. Thus, $\sigma_A^2(n)$ and $\sigma_D^2(n)$ reflect the same ensemble-mean GW variance with the same mean net eastward/westward propagation component $\sigma_{EW}^2(n)$. With these assumptions, Eqs. (2a) and (2b) reveal that the ascending minus descending variance $\sigma_A^2(n) - \sigma_D^2(n)$ can be used to estimate the variance asymmetry between southward- and northward-propagating GW components, $\sigma_S^2(n) - \sigma_N^2(n)$. Thus, a positive ascending minus descending (A − D) variance suggests dominance of GWs with a southward component to their wave propagation, relative to those with a northward component.

At mid and high latitudes, the $\sigma_{EW}^2(n)$ component in Eqs. (2a) and (2b) will become larger as the MLS LOS deviates further from the meridional plane (to ~16.7° at ±60° latitude; see Fig. 2b). Nonetheless, as long as the mean GW ensemble sampled by the ascending and descending orbits is the same, the A − D variance remains a good proxy for the asymmetry in variance between GWs with southward and northward components to their horizontal phase propagation. Note that any systematic mean diurnal variation in GW variance is neglected in this interpretation of the A − D variance.

d. Sensitivity to short vertical wavelengths

High-resolution suborbital observations suggest that GW temperature variances in the stratosphere are dominated by GWs with vertical wavelengths between 2 and 10 km (e.g., Tsuda et al. 1991; Allen and Vincent 1995; Whiteway 1999). Therefore, it is important to determine precisely the MLS sensitivity to GWs at these short vertical wavelengths. The visibility simulations in Fig. 3a reveal that 1-K temperature perturbations induced by GWs of $\lambda_z = 5$ km and $\lambda_y \approx 50$–100 km can produce a radiance variance of ~0.02 K^2. Although weak, such a variance is certainly measurable by *Aura* MLS because of the low instrument noise. As indicated in Table 1, the MLS radiometric noise in channel 1(25) allows a GW variance of $\geq 2.3 \times 10^{-3}$ K^2 to be detected in a 5° × 10° monthly map or in daily zonal averages with 5° latitude bins. Moreover, a 0.02 K^2 GW variance can even show up in a 5-day 5° × 10° map for channel 1(25), in which the estimated noise floor in Table 1 is $\sim 5.6 \times 10^{-3}$ K^2. GW observations at 5-day temporal resolution or better are often needed to monitor transient GW events like those reported by Wu and Zhang (2004) and Eckermann et al. (2006b).

These noise and visibility estimates confirm that the *Aura* MLS sensitivity to GWs at short vertical wavelengths is greatly improved over the UARS MLS, due mainly to the narrower beamwidth (i.e., vertical FOV) of the new instrument. In particular, for waves with $\lambda_z = 5$ km, the *Aura* MLS vertical FOV of 0.113° provides two orders of magnitude greater sensitivity than the *UARS* MLS.

4. Initial results from the *Aura* MLS

a. Zonal mean variances

Figures 4 and 5 show zonal mean ascending and descending GW variances and the A − D variance differences from the *Aura* MLS for January and July 2005, respectively. Despite instrumental and viewing/sampling differences, the morphology of these *Aura* MLS GW variances is very similar to that of the corresponding *UARS* MLS variances at altitudes above 30 km for 1992–93 (Wu and Waters 1996). Increased zonal-mean GW variances in Figs. 4a and 5a correlate well with corresponding increases in the zonal-mean zonal wind speeds in the stratosphere, showing large variances at winter high latitudes within the summer and winter stratospheric jets. These correlations follow from the hydrostatic nonrotating GW dispersion relation, in which the vertical wavelength refracts in the presence of background winds and temperatures as

$$\lambda_z = \frac{2\pi|c - U\cos\varphi|}{N}, \tag{3}$$

where c is the ground-based horizontal phase speed, U is the background wind speed, N is the background BV frequency, and φ is the difference between the wind vector and GW horizontal propagation directions. Extratropical stratospheric wind jet speeds $|U|$ are large and increase with height, causing some GWs to refract to critical levels ($\lambda_z \rightarrow 0$) where they are removed and others to refract via Eq. (3) to long vertical wavelengths and to propagate rapidly through the stratosphere. This can have two potential effects on the variance observed by MLS. First, the waves refracted to long λ_z become much more visible to MLS, whereas those refracted toward critical levels soon become invisible (see Fig. 3). Second, a high background wind can allow more waves with low phase speeds c to propagate through the stratosphere because they will not encounter stratospheric critical levels. For example, most orographic GWs are generated with low phase speeds c, and therefore more wave energy is likely to propagate upward in regions where background winds are strong. Both effects can enhance measured variances and must be carefully separated.

For example, *UARS* MLS GW variances exhibited strong correlations with background wind speeds be-

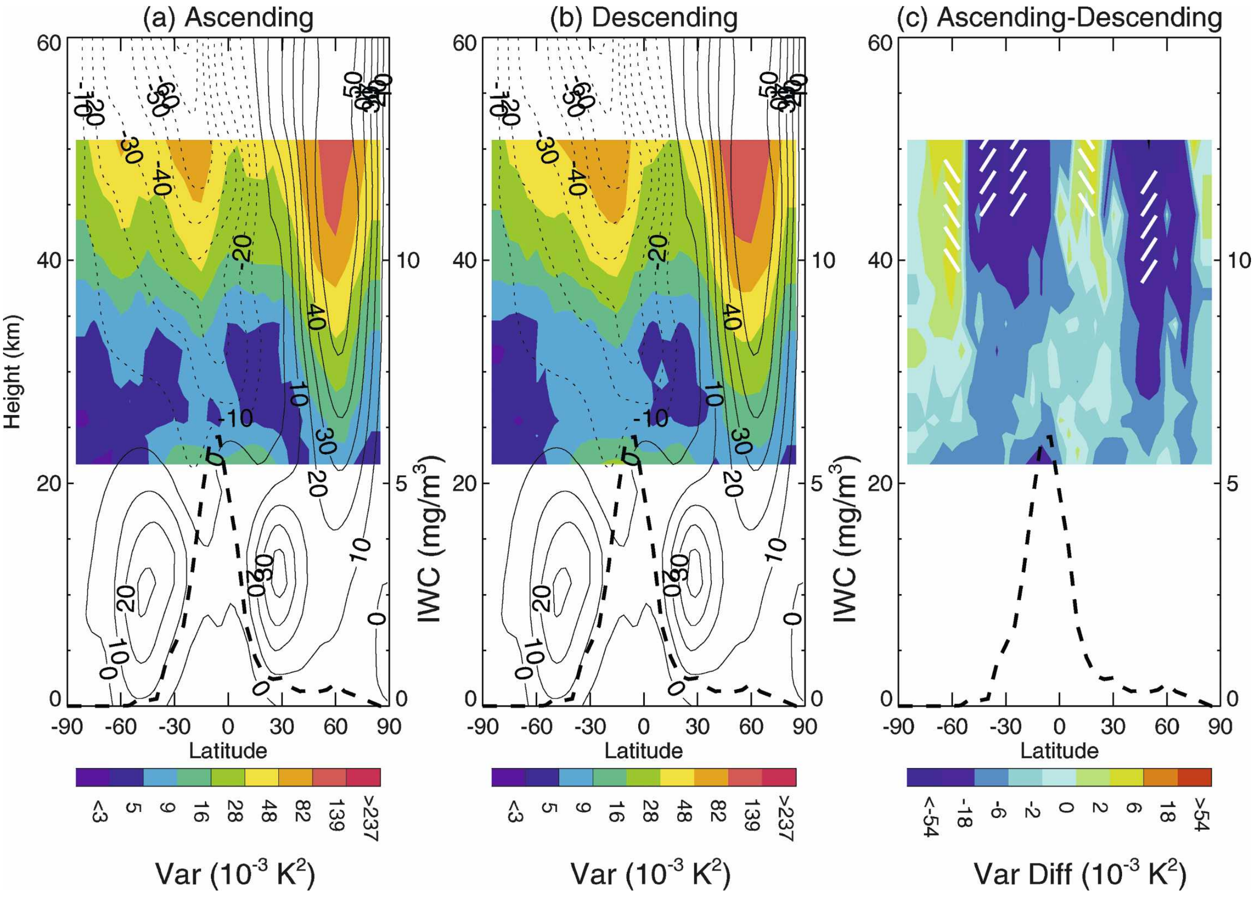

FIG. 4. Latitude–height distribution of the zonal-mean MLS GW variance from (a) ascending and (b) descending orbits for January 2005. Contours are the zonal mean zonal winds from the Met Office analysis (dotted westward; solid eastward; contour labels in meters per second) and the bold dotted line is the simultaneous MLS ice water content (IWC) with the scale on the right axis. (c) Zonal-mean GW variance differences between ascending and descending orbits. The overplotted white lines schematically depict the wave phase orientation inferred from the statistically significant A − D variance differences (southward for A − D > 0 and northward for A − D < 0).

cause of the far greater overall visibility of the GW spectrum to MLS in regions with fast background winds (Alexander 1998). These strong effects had to be carefully accounted for to isolate additional signals in the variances from wave sources such as mountains and convection (e.g., McLandress et al. 2000; Jiang et al. 2004a). On the other hand, GW variances from satellite instruments with higher vertical resolution suffer less from this effect by resolving a wider range of vertical wavelengths (e.g., Tsuda et al. 2000; Preusse et al. 2006). Of particular interest here is to assess how the much improved vertical resolution of the *Aura* MLS impacts direct detection of geophysical GW variance signals compared to the *UARS* MLS.

In Figs. 4 and 5 the MLS GW variances show a general increase with height at all latitudes. One important exception is in the tropical and subtropical lower stratosphere, where variances are larger than those values immediately above and poleward. Equatorially confined enhancements in lower stratospheric GW temperature variance like these have been observed previously in high–vertical resolution satellite limb data (e.g., Fetzer and Gille 1994; Preusse et al. 2000; Tsuda et al. 2000, 2004; Ratnam et al. 2004) and suborbital profile data (Eckermann et al. 1995; Allen and Vincent 1995). This tropical enhancement is not present in UARS MLS variances (see, e.g., Fig. 12 of Wu and Waters 1997) because the instrument did not have a frequency bandwidth sufficient to observe altitudes below 28 km, where this feature appears most strongly. Work by Preusse et al. (2000) suggested that the coarse *UARS* MLS vertical WFs could not resolve this equatorial enhancement even if its channels extended to these lower altitudes. Thus, its occurrence in *Aura* MLS variances provides a clear demonstration of the much improved sensitivity of this new MLS instrument to short GW vertical wavelengths, as described in section 3d.

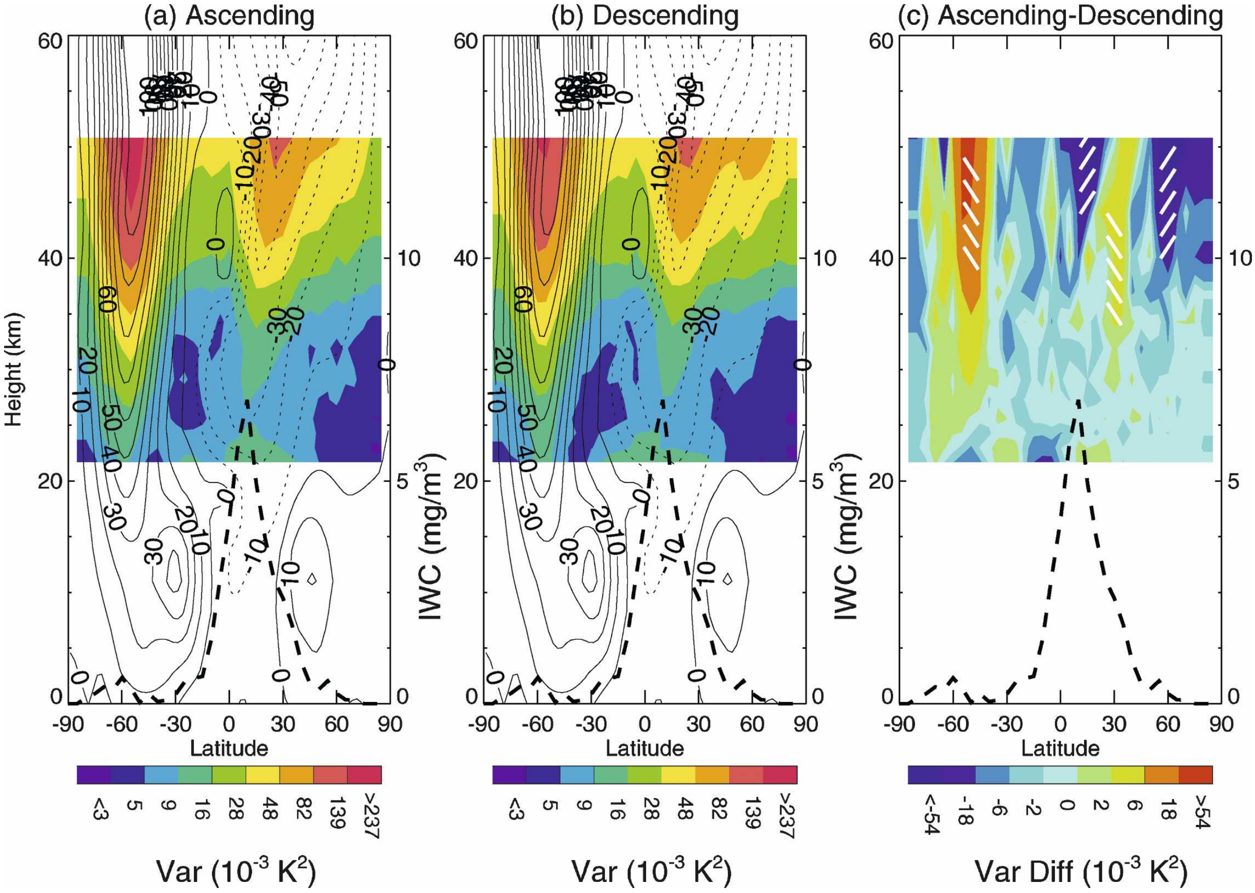

FIG. 5. As in Fig. 4, but for July 2005.

Nonetheless, we do not see a latitudinally symmetric equatorial variance enhancement in the lower stratosphere. The variances in January 2005 exhibit slight double peaks at ±20° latitudes where the background wind speeds have local maxima, whereas the relatively lower equatorial variance is associated with a weak eastward background wind and a deep convection peak (as indicated by MLS cloud ice observations; Wu et al. 2006b), which are plotted as the dashed curves in Figs. 4 and 5. In July 2005, the subtropical enhancement at 21–25 km is confined to northern latitudes, which correlates well with enhanced wind speeds and deep convection at these latitudes, a feature previously reported in *UARS* MLS variances by Jiang et al. (2004b).

Two main theories for the equatorial enhancement in lower stratospheric GW variance have been proposed. Eckermann (1995) interpreted the observed feature in rocket data as equatorial trapping of short-λ_z Kelvin modes. Alexander et al. (2002) attributed it to enhanced variances in short-λ_z low-frequency GWs that are supported at tropical latitudes by the decrease in inertial frequency that expands the range of allowed GW propagating frequencies. Interestingly, both theories interpret the enhanced variance as resulting from more waves with long horizontal wavelengths and low intrinsic frequencies near the equator, to which these 40-pt MLS variances are largely insensitive (see section 3b). The fact that an equatorial peak arises in these shorter-scale higher-frequency MLS GW variances too suggests that this feature observed by MLS may reflect a more general tropical enhancement in lower-stratospheric GW variances at all wavelength scales, possibly due to enhanced GW generation correlated with tropical tropospheric cloud ice (dotted curves in Figs. 4 and 5) and associated deep convection.

To infer meridional wave propagation anisotropies, zonal-mean A − D variances are plotted in Figs. 4c and 5c for January and July 2005, respectively. Assuming upward GW group propagation, the white lines superimposed on the statistically significant positive and negative A − D values (see Table 1) depict the GW phase structures that are implied. In January 2005 (Fig. 4c), GWs near 40°–60°N show a preference for a northward component of propagation $[\sigma_A^2(n) - \sigma_D^2(n) < 0]$

into the core of the strong upper stratospheric polar jet. This result is consistent with the conclusion inferred from *UARS* MLS limb-tracking GW variances in northern high-latitude winter by Jiang and Wu (2001), who found a strong cross-jet-propagating GW component near the vortex edge. However, because of aliasing associated with *UARS* MLS sampling, their study could not identify absolute GW propagation directions. The *Aura* MLS $\sigma_A^2(n) - \sigma_D^2(n)$ maps confirm the presence of cross-jet-propagating GWs near the vortex edge and suggest that waves here propagate preferentially northward on average. At 10°S–40°S and 10°–20°N equatorward propagation components are preferred, whereas at latitudes south of 60°S, although the GW variances are weak, there is an overall tendency toward net southward propagation.

Similar poleward propagation tendencies at high latitudes are revealed in July 2005 (Fig. 5c). However, in the northern subtropics the inferred meridional propagation anisotropies are somewhat different from those in the southern subtropics for the opposite season (January 2005). Below 40 km, southward propagation components are preferred, but above 40 km we infer dominant southward propagation at 60°–40°S and 30°–40°N and net northward propagation components at 10°–20°N and 50°–70°N.

Although the *UARS* and *Aura* MLS observe similar zonal mean climatologies of GW variance, the *Aura* MLS variances are 5–8 times larger than the *UARS* MLS values in the middle stratosphere, partly because of the greater sensitivity of the *Aura* MLS to GWs with 2–10-km vertical wavelengths, which dominate GW-induced stratospheric temperature variability. UARS MLS variances are also found to be weaker (by a factor of ~10) than AMSU-A variances at similar altitudes (Wu 2004) because of different horizontal truncations used in the variance computations.

b. Monthly maps

Figures 6 and 7 plot monthly-mean global maps of $\sigma_A^2(n)$, $\sigma_D^2(n)$, and $\sigma_A^2(n) - \sigma_D^2(n)$ for different channels n that saturate at altitudes ranging from the lower to the upper stratosphere. Like the zonal means in Figs. 4a and 4b, the $\sigma_A^2(n)$ and $\sigma_D^2(n)$ maps in January 2005 (Fig. 6) show significant enhancements at latitudes of the winter polar and the summer subtropical stratospheric jets. As discussed in section 4a, these latitudinal enhancements can be explained by the effects of wave refraction by the background wind, in which GWs attaining long vertical wavelengths in these high-wind regions become more visible to the MLS. However, Fig. 6 shows that these enhancements are zonally asymmetric, which (as with similar features in *UARS* MLS maps) reveals the significant modulation of wave visibility by zonal asymmetries in stratospheric wind speeds as well as underlying wave sources (McLandress et al. 2000). Along the vortex edge, for instance, localized variance enhancements are closely tied to significant underlying topography in Alaska, Canada, southern Greenland, Scandinavia, and the Alps, suggesting these are due to large-amplitude orographic gravity waves. Detailed data analysis and global modeling by Jiang et al. (2004a) identified these and other Northern Hemisphere (NH) mountain ranges as sources of enhanced *UARS* MLS stratospheric radiance variance.

Although the zonal-mean $\sigma_A^2(n) - \sigma_D^2(n)$ in Fig. 4c suggested mean poleward propagation at 40°–60°N, the corresponding map in Fig. 6 reveals substantial zonal variability. GWs over Alaska, the east coast of the United States, southern Scandinavia, and the Alps have preferred northward propagation components [$\sigma_A^2(n) - \sigma_D^2(n) < 0$], whereas variance peaks over the Rockies and southern Greenland are dominated by waves with southward components to their propagation [$\sigma_A^2(n) - \sigma_D^2(n) > 0$].

In the subtropics, the $\sigma_A^2(n)$ and $\sigma_D^2(n)$ enhancements correlate well with the MLS cloud ice distribution (white contours in Fig. 6), suggesting deep tropospheric convection over major landmasses and the Maritime Continent as the primary source of these regional variance increases. Similar features and correlations to tropical convection were noted in *UARS* MLS variances by McLandress et al. (2000) and Jiang et al. (2004b, 2005). As observed with the *UARS* MLS (Jiang et al. 2004b), the locations of upper stratospheric variance enhancements from convectively generated GWs are shifted slightly southeastward from the convective centers as waves propagate upward from the forcing region. The filtering and refraction of GWs by the subtropical stratospheric jet can explain most of this shifted distribution because the jet core tilts away from the equator with altitude. However, it remains puzzling that the A − D maps in Fig. 6 suggest that these waves have preferred northward propagation components [$\sigma_A^2(n) - \sigma_D^2(n) < 0$] rather than southward ones in these regions.

Like the zonal means in Fig. 5a, global maps for July 2005 in Fig. 7 again show variances in the upper stratosphere that are enhanced at latitudes at which background wind speeds are large, specifically along the winter polar stratospheric jet and over subtropical monsoons. The vortex enhancements show a nonuniform distribution in longitude with the highest variances near the southern tip of South America and the Antarctic Peninsula, a feature associated with large-amplitude orographic GWs that have been observed in these re-

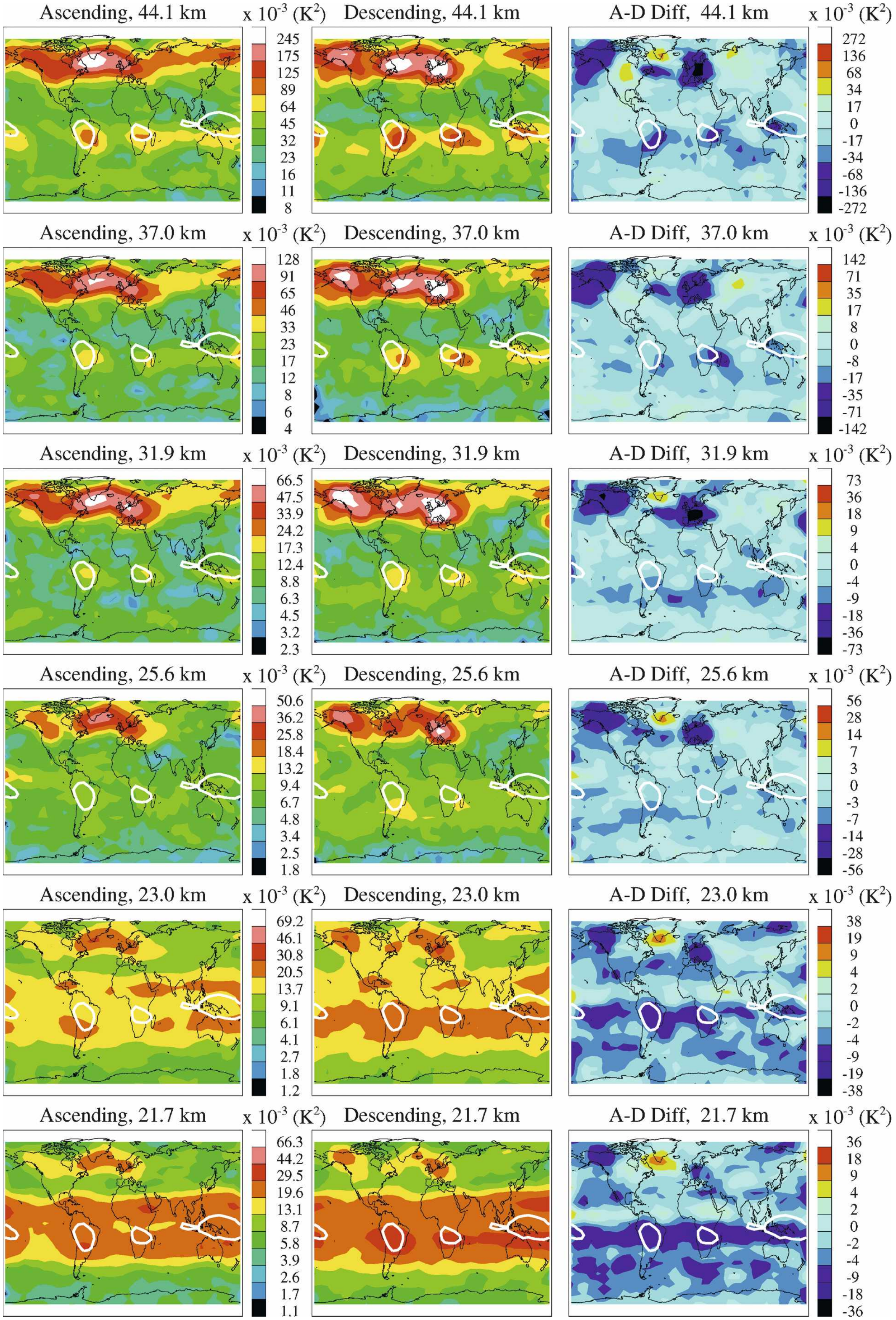

FIG. 6. MLS GW variance maps for January 2005, showing (left) ascending, (middle) descending, and (right) A − D differences for selected channels. The white contours are 5 mg m^{-3} of MLS IWC as an indicator of deep convective forcing. Both ascending and descending maps share the same color scale, whereas the A − D maps use the scale to the right.

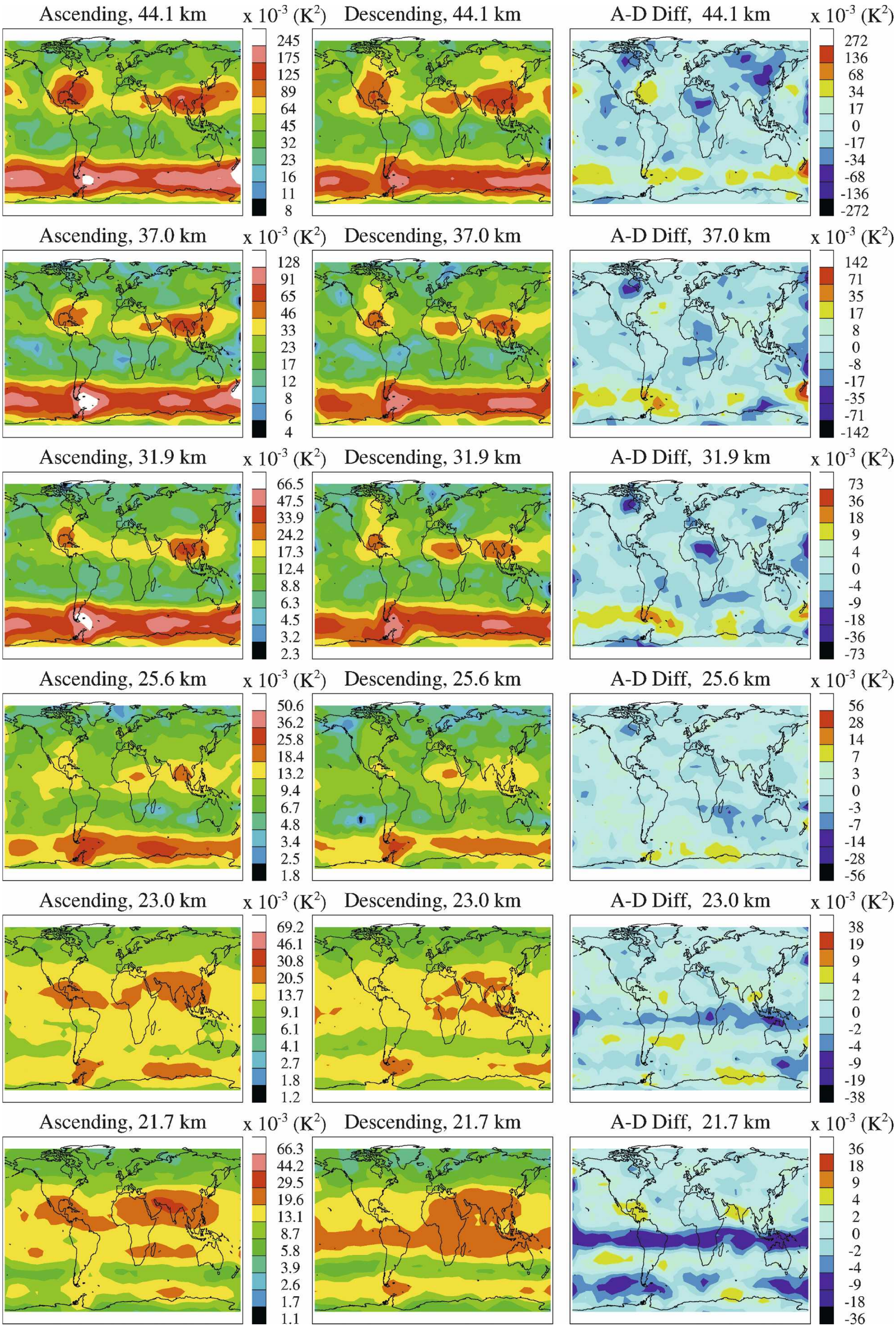

FIG. 7. As in Fig. 6, but for July 2005.

gions by a number of other satellite instruments (Eckermann and Preusse 1999; McLandress et al. 2000; Tsuda et al. 2000; Preusse et al. 2002; Jiang and Wu 2001; Jiang et al. 2002; Alexander and Teitelbaum 2007). Enhanced variance due to orographic GWs is also observed over New Zealand at altitudes >30 km, as was seen in *UARS* MLS radiance variances (Jiang et al. 2005). Broader vortex enhancements are also seen in regions well away from significant mountains, which may result in part from GWs radiated from imbalances within baroclinic jet/front systems at these latitudes (e.g., Guest et al. 2000; see section 5). The corresponding A − D variance maps in Fig. 7 suggest a net poleward propagation tendency $[\sigma_A^2(n) - \sigma_D^2(n) > 0]$ in the upper stratosphere for this southern high-latitude band, consistent with the zonal means in Fig. 5c.

The pockets of enhanced variances in the northern subtropics seem to be mostly associated with American and Indian monsoon systems and again correlate well with similar enhancements in MLS cloud ice (white contours in Fig. 7). There is little latitudinal shift between the variance peak and deep convection in the Indian monsoon. However, the latitudinal shift over the American monsoon is significant, showing the variance peak displaced to the northeast from the deep convection center, and the displacement increases with height. However, the A − D difference maps in Fig. 7 suggest that these GWs over the southeastern United States preferentially propagate to the south, rather than northward from convection centers. High-resolution radiosonde data also show a lower stratospheric GW variance enhancement over the southeastern United States (Wang and Geller 2003), with a preference for northward-eastward propagation in June–August (Wang 2003). However, Wang et al. (2005) also inferred long horizontal wavelengths (>~500 km) and low intrinsic frequencies for these GWs. The GWs resolved in the MLS variances have much shorter horizontal wavelengths and higher intrinsic frequencies and so may have fundamentally different sources and propagation characteristics. Thus, the MLS GW activity in this region merits further investigation. For example, a similar feature is also seen in the Pacific just east of Japan in Fig. 7. Climatologically, both regions experience typhoon/hurricane passages, which may generate some of this net southward-propagating stratospheric GW variance observed by the MLS (e.g., Sato 1993; Kim et al. 2005).

The bottom panels of Fig. 6 show that the ascending variance at 21.7-km altitude in January 2005 has lower values in the equatorial band relative to the descending variance and peaks in two subtropical bands (see also Fig. 4a), similar to tropical GW activity seen in GPS/Challenging Minisatellite Payload (CHAMP) data during May 2001–January 2003 (Ratnam et al. 2004). The resulting subtropical A − D variances at 21.7 km in Fig. 6 are positive in the north and negative in the south (see also Fig. 4c), suggesting that the net meridional component of propagation of subtropical GWs observable by MLS in the lower stratosphere in January 2005 is equatorward in both hemispheres. However, the situation is quite different in January 2006 when the descending variances at 21.7 km exceed the ascending variances almost everywhere in the tropics (see also Fig. 8), implying widespread northward propagation components, and thus possible GW–quasi-biennial oscillation (QBO) interactions here (e.g., Eckermann et al. 1995; Vincent and Alexander 2000; Wang and Geller 2003). We investigate this further in section 4c. Over Indonesia and northern Australia, where GWs are presumably generated by active convective systems in the region (Tsuda et al. 2004), the A − D variances at 21.7 km in Fig. 6 suggest preferred northward propagation. Using a 3D mesoscale cloud-resolving model with realistic heating and background meteorological inputs, Alexander et al. (2004) found that convectively generated GWs near Darwin, Australia were dominated by northeastward propagation in November 2001. Their finding is consistent with the MLS climatology in November (see Fig. 8), which also exhibits negative A − D variances at 21.7 km in the Darwin region. However, over the Australian continent waves are dominated by southward propagation.

In July 2005, the subtropical A − D variances at 21.7-km altitude (Fig. 7) also show preferences for equatorward propagation components. The equatorial variance peaks at 21.7 km are displaced northward (see also Fig. 5a) because seasonal convective sources are mostly located on the summer side of the tropics. At higher altitudes, these subtropical peaks move further to the north, consistent with similar northward displacement with the height of the core of the subtropical jet. The July 2006 variance maps in Fig. 8 exhibit a similar morphology.

c. Seasonal variations

Figure 8 plots monthly-mean variances at 21.7 km for each month of 2006. Because of QBO modulation, the tropical variances are larger in early 2006 when the QBO is in the easterly (westward) phase. In January 2006, GW variance maximizes near the equator with slight longitudinal variations, with secondary high-latitude peaks occurring over Greenland and Europe. As the QBO changes to the westerly phase, the tropical variance starts to split into two latitudinal bands after June 2006. By August–October the equatorial variances have weakened substantially and variance maps

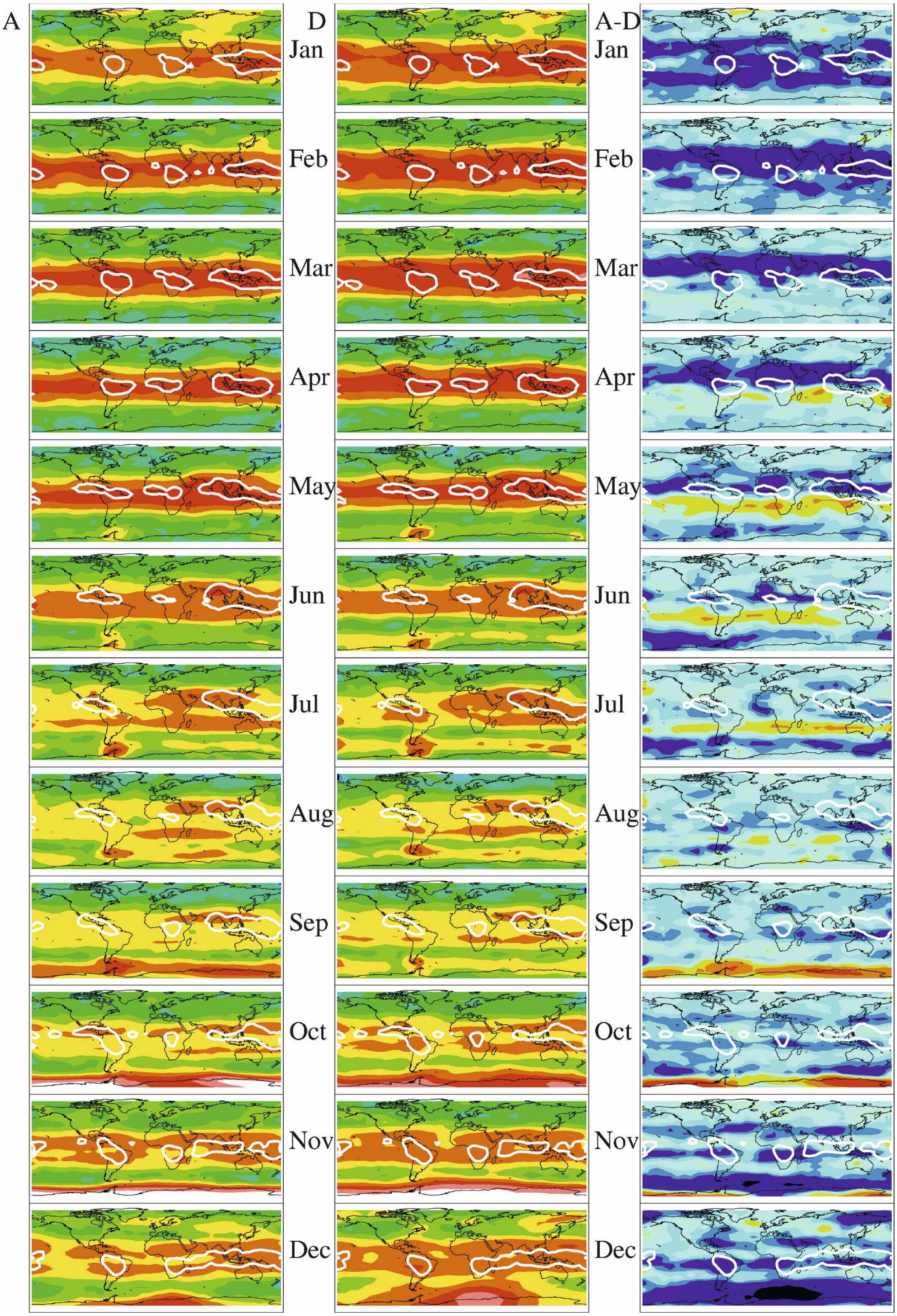

FIG. 8. Monthly maps of the ascending, descending, and A − D variances at ~21.7-km pressure altitude for 2006. The color scales, ranges, and contours have their same values and meaning as in the 21.7-km altitude panels in Figs. 6–7.

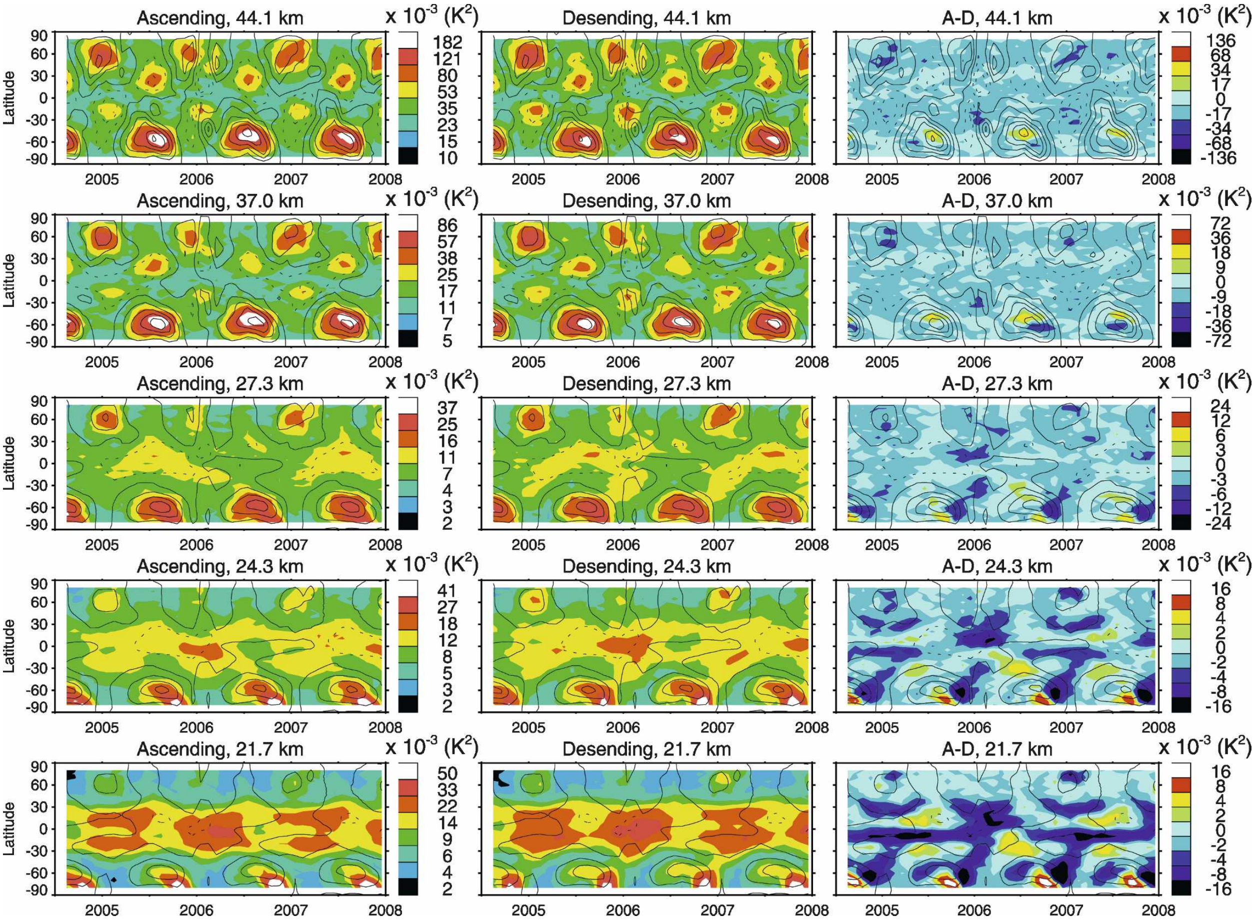

FIG. 9. Time series of monthly zonal-mean ascending, descending, and A − D variances at selected altitudes. Color scales and units for ascending and descending variances are given by the common color bar between each panel, and for A − D variances by the color bar to the far right. The tick marks associated with year label on the time axis indicate the beginning of that year. Overlaid contours depict the mean zonal wind from the Met Office analysis at intervals of 20 m s^{-1}, with dashed (solid) lines indicating westward (eastward) winds.

are dominated by enhancements over southern South America, Antarctica, and the Southern Ocean.

Figure 9 shows a time series of monthly zonal mean $\sigma_A^2(n)$ and $\sigma_D^2(n)$ and their difference as a function of latitude at selected altitudes. The major annual and vertical variations are controlled by seasonally varying background winds, which filter some GWs and refract others via Eq. (3) to long (short) vertical wavelengths that are more (less) visible to the instrument (Alexander 1998). Although MLS GW variances are dominated by these annual variations, there is also a clear correlation between the QBO and MLS GW variances in the tropical lower stratosphere, most noticeably in Fig. 9 at 27.3-km altitude (~20 hPa), where the amplitude of the zonal wind QBO peaks (Baldwin et al. 2001). At 21.7-km altitude, the tropical GW variance in Fig. 9 exhibits a latitudinal distribution with double peaks in 2004–05 during a westerly QBO phase but a broad equatorially centered peak in 2005–06 during an easterly QBO phase. The A − D variances at 15°S–15°N show net equatorward propagation during the westerly to easterly (W→E) QBO transition and net poleward propagation during the E→W transition. It is worth noting that AMSU-A, using the method described by Wu (2004), cannot observe this tropical GW activity although it has a WF similar to the *Aura* MLS at these altitudes. The viewing geometry, FOV width, and instrument sensitivity of *Aura* MLS must play a critical role in the detection of such waves.

It is not yet clear what causes the double-peak structure in the 2004–05 GW distribution. However, the QBO wind filtering and different GW modes may explain the observed features. Because MLS GW variances (from waves of long vertical and short horizontal wavelengths) are particularly sensitive to the background winds, the QBO in the zonal wind could regulate the observed variance substantially if the variance is dominated by waves propagating in a zonal direction (i.e., eastward or westward). Thus, the observed double-peak distribution and associated A − D variation suggest that the observed waves are mostly eastward-propagating, which would suffer from the filtering by the westerly QBO shear and result in the split latitudinal distribution. This inference from MLS is consistent with radiosonde observations during the easterly QBO, showing predominant eastward-propagating inertia GWs in the subtropics (e.g., Wada et al. 1999) and weak wave activity in the tropics (Sato and Dunkerton 1997). On the other hand, waves may be excited with different modes in the upper troposphere, but little study has been done on what kinds of wave modes, especially in mesoscale, are generated during different QBO phases. Nevertheless, the cause–effect relation between the QBO and the GWs observed by MLS remains unclear and warrants further investigations with dedicated GW modeling studies.

The equatorial GW variances at 21.7, 24.3, and 27.1 km in Fig. 9 all peak when the easterly phase of the QBO reaches its maximum. Rocketsonde, radiosonde, and satellite limb temperatures also find equatorial GW variances peaking during periods of strong QBO easterlies and indicate that wave variances are suppressed immediately above in descending westerly QBO shear zones (Eckermann et al. 1995; Sato and Dunkerton 1997; Vincent and Alexander 2000; Randel and Wu 2005; Wu 2006; de la Torre et al. 2006; Krebsbach and Preusse 2007).

Figure 9 also reveals variance enhancements at 21–25 km altitude at 70°–80°S that occur around October–November of each year. These enhancements are particularly interesting because they do not correlate with corresponding increases in the zonal-mean zonal winds, like GW enhancements at other latitudes, heights, and times. Inspection of raw maps at these times (in addition to Fig. 8) reveals variance enhancements at pressure altitudes below 30 km over a broad area of the Antarctic continent as the vortex shifts off the pole during the vortex breakup season. Large increases in GW temperature variance at ~20-km altitude over Antarctica during late spring have previously been reported using radiosonde data (Pfenninger et al. 1999; Yoshiki and Sato 2000; Yoshiki et al. 2004) and GPS/CHAMP occultation data (Baumgaertner and McDonald 2007). Above 20–25 km, the peak GW variances in these studies tend to occur in midwinter (Yoshiki and Sato 2000; Baumgaertner and McDonald 2007), also in agreement with the MLS GW variances in Fig. 9.

In the middle and upper stratosphere the latitude–season trends of GW variances (e.g., at 44.1 km in Fig. 9) are very similar to those seen in UARS MLS variances (Wu and Waters 1997), showing a dominant annual variation at latitudes poleward of 30°. In the tropics, the QBO modulation seen lower down weakens and gives way to weaker modulation by the tropical stratospheric semiannual oscillation (SAO) in the upper stratosphere, in agreement with equatorial GW temperature variances from suborbital data (e.g., Eckermann et al. 1995). The extratropical wave variances are generally larger in the Southern Hemisphere (SH) than those in the NH for both ascending and descending measurements, which may be a visibility effect due to generally stronger stratospheric wind jets in the SH.

Figure 9 shows considerable differences in high-latitude variance between different northern winters, consistent with the well-known interannual variability of the entire Arctic winter stratosphere. Qualitatively similar interannual variability in high-latitude *UARS* MLS GW variance was studied by Jiang et al. (2006). Because disturbed (undisturbed) polar vortex conditions manifest as weakened (strengthened) background wind speeds, which in turn control the visibility of GWs to MLS (Alexander 1998), much of the interannual variation in Fig. 9 may be a visibility effect controlled by interannual variations in the strength of vortex winds. For example, the northern winter stratosphere in February 2006 experienced a major warming that led to extremely weak stratospheric zonal-mean zonal wind speeds compared to more typical conditions in February 2005, which may explain (via GW visibility arguments) the smaller northern polar winter MLS variances in 2005 compared to 2006 in Fig. 9. However, analysis of SABER temperature data and global modeling by Siskind et al. (2007) suggests that the weakened 2006 vortex filtered out most orographic gravity waves, yielding a much-reduced upper-level orographic gravity wave drag relative to 2005, which then led to an anomalously strong lower-mesospheric vortex in 2006. Reductions in stratospheric GW temperature variances during stratospheric warmings have also been reported in ground-based studies (e.g., Whiteway and Carswell 1994). Thus, the relative roles of wind filtering and real changes in stratospheric GW activity in forming the interannual GW variances in Fig. 9 during northern polar winter merit further investigation and will be a focus of future research.

5. Comparisons with ECMWF analyses

To help assess some of our inferences about the sensitivity of the *Aura* MLS to different GW wavelengths, sources, and propagation directions, we utilize as pre-

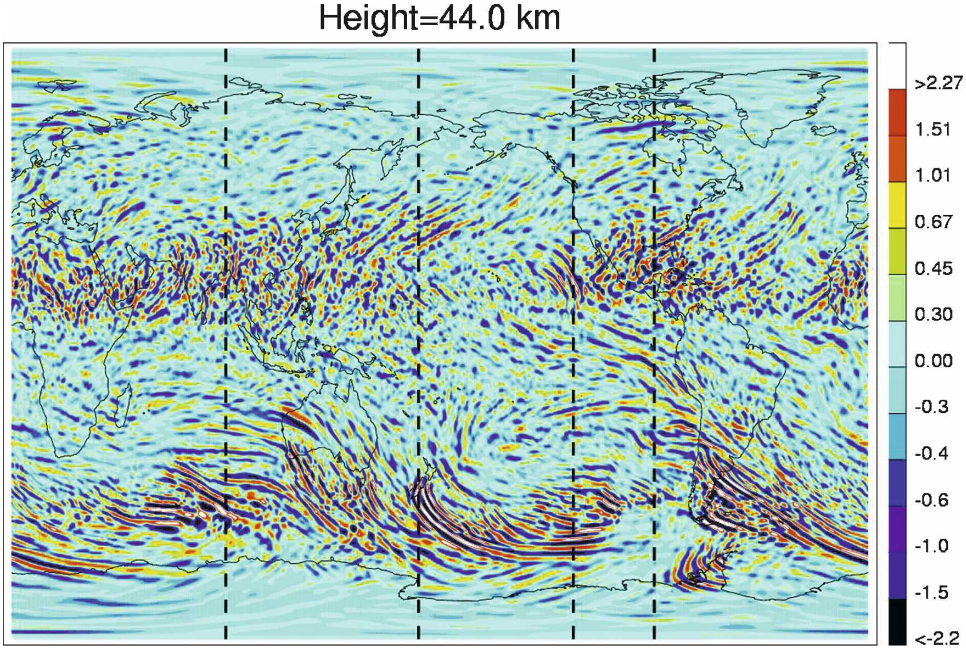

FIG. 10. Temperature perturbation map (K) from the ECMWF $T_L799L91$ analysis fields at 44-km pressure altitude at 0000 UTC 20 Aug 2006. A 2D horizontal high-pass filter was applied to extract the small-scale structure, which corresponds to a long wavelength cutoff of ~300 km at low and middle latitudes. Dotted lines indicate the cross sections to be shown in Fig. 11 at 82°E, 171°E, 236°E, and 297°E.

liminary modeling support some high-resolution global analysis fields issued operationally by ECMWF IFS. We use global fields at the native $T_L799L91$ model resolution, corresponding to ~25-km horizontal gridpoint resolution on the reduced linear Gaussian grid. The 91 vertical model layers have a resolution of ~0.4 km in the lower stratosphere, increasing to ~1 km near ~30-km altitude and ~2 km at ~45-km altitude.

To first order, these nominal horizontal and vertical gridpoint resolutions act like the 3D WFs for the *Aura* MLS in determining which GWs the ECMWF IFS fields can and cannot explicitly simulate (the precise sensitivities to GWs are much more complex, depending on other model specifics, such as the amount of spectral hyperdiffusion applied to model divergence fields in the stratosphere). Thus, like the MLS, the ECMWF IFS will tend to resolve GWs better in strong wind environments in which vertical wavelengths become long. Indeed, earlier lower-resolution versions of ECMWF IFS forecast/analysis fields have revealed explicitly resolved gravity waves in the stratosphere within strong winds located near the polar vortex edge associated with orography (e.g., Hertzog et al. 2002; Eckermann et al. 2006a,b; Alexander and Teitelbaum 2007) and jet stream instabilities (Hertzog et al. 2001; Plougonven and Teitelbaum 2003). Thus, these higher-resolution IFS fields should resolve even more stratospheric GW activity.

We begin by studying the analyzed ECMWF IFS temperature fields at one particular day and time (0000 UTC 21 August 2006). We remove wave components with horizontal scales longer than ~300 km to roughly mimic maximum resolved scales in the 40-pt MLS variances. No vertical filtering is applied in this initial analysis, which may produce larger GW variances than in the MLS variances by retaining GWs with vertical wavelengths that MLS either cannot resolve or resolves with significantly reduced amplitude because of WF smearing. However, because the IFS vertical resolution is ~2 km at 45-km altitude, the model fields here cannot resolve GWs with vertical wavelengths shorter than ~4–6 km. Thus, the IFS fields at 45 km have an intrinsic short-λ_z cutoff that is similar to the MLS 40-pt variances (see Fig. 3a).

Figure 10 shows a global map of the instantaneous IFS temperature perturbation oscillations at ~44-km pressure altitude (assuming a constant scale height of 6.95 km); Fig. 11 plots latitude–height cross sections of these oscillations at selected longitudes marked with dotted lines in Fig. 10. As with the *Aura* MLS variances in Figs. 5 and 7, the perturbation amplitudes in Fig. 10 peak near the edge of the southern polar vortex and the

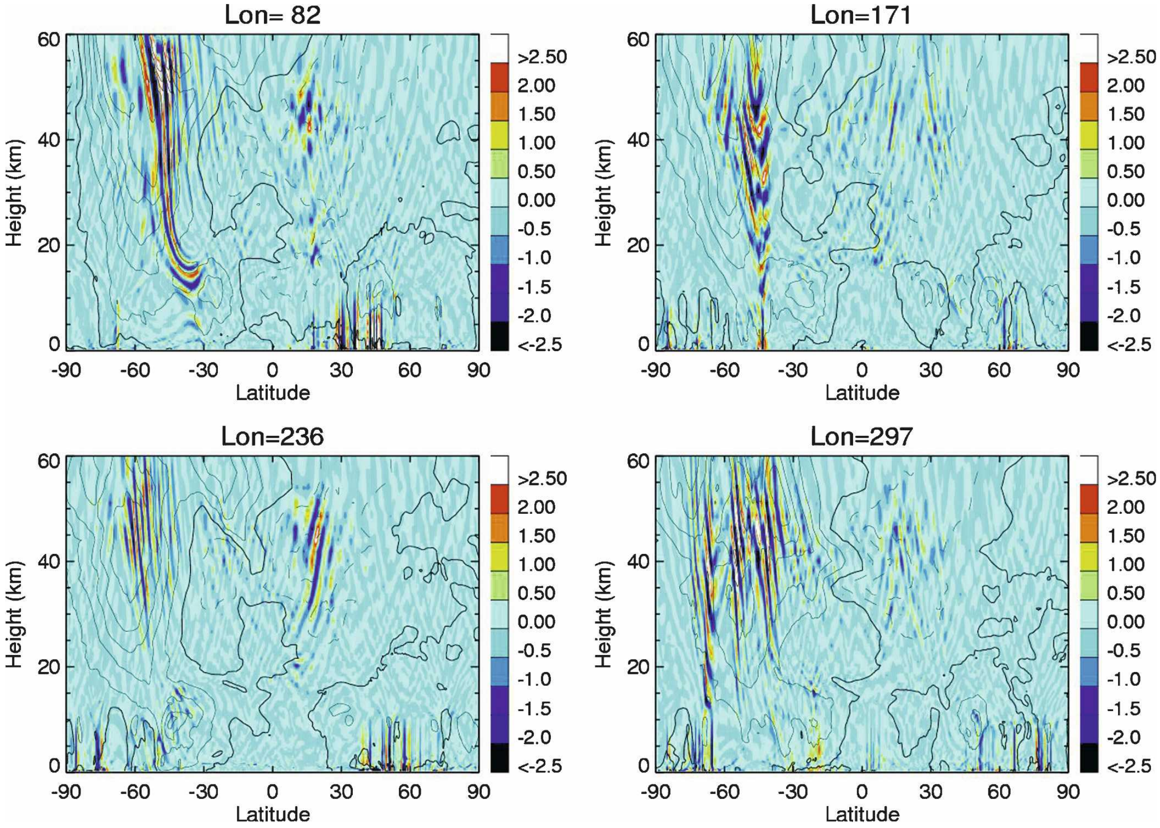

FIG. 11. Cross sections of temperature perturbations (K; see color bars) as a function of latitude and pressure altitude from the ECMWF T_L799L91 analysis fields at 0000 UTC 20 Aug 2006 at the selected longitudes shown in the title (in degrees east) and highlighted in Fig. 10. Contours lines are the background zonal winds from the ECMWF IFS analysis at that longitude and have increments of 10 m s^{-1} with dashed (solid) lines denoting westward (eastward) values.

northern subtropics, where background winds are strongest and GW vertical wavelengths are longest and thus easiest for the IFS to resolve. Near the southern vortex edge, enhanced-amplitude perturbations due to mountain waves are evident over southern South America, the Antarctic Peninsula, and New Zealand, but significant enhancements also occur over broader regions of the Southern Ocean well away from any mountains. The cross sections in Fig. 11 show some of this GW activity emanating from tropopause altitudes, presumably radiated from tropospheric jet stream instabilities associated with baroclinic storm systems that regularly form and propagate across the Southern Ocean (O'Sullivan and Dunkerton 1995; Guest et al. 2000). The cross sections in Fig. 11 show that the explicitly simulated GWs at 40°–80°S from both the jet and mountain sources exhibit wave phases that tilt upward toward the South Pole, consistent with the predominant southward GW group propagation directions inferred from MLS A − D variance difference maps in Figs. 5 and 7.

Enhanced ECMWF IFS temperature perturbation amplitudes in the northern subtropical upper stratosphere in Fig. 10 exhibit a shorter-scale, more disorganized structure with less horizontal coherence, superficially consistent with episodic localized generation from deep tropospheric convection. For example, the cross section at 236°E in Fig. 11 shows weaker-amplitude GWs radiated into the stratosphere at ~10°–20°S, a region over open ocean off the west coast of Mexico where enhanced GW activity is seen in Fig. 10. Because tropical cyclones are known to be sources of stratospheric GWs (e.g., Sato 1993; Chane-Ming et al. 2002; Kim et al. 2005), these GWs were presumably generated in the IFS by Hurricane Hector, whose eye was near (18.3°N, 229°E) at this time and thus directly beneath the GW activity in Fig. 10.

Figure 12b plots a map of the monthly-mean analyzed ECMWF IFS temperature variance at 44-km pressure altitude in August 2006; Fig. 12a shows the corresponding 40-pt *Aura* MLS ascending radiance variance at ~44 km. There is general agreement between the two maps in terms of both geographical variability and variance level. As with the MLS, the wave

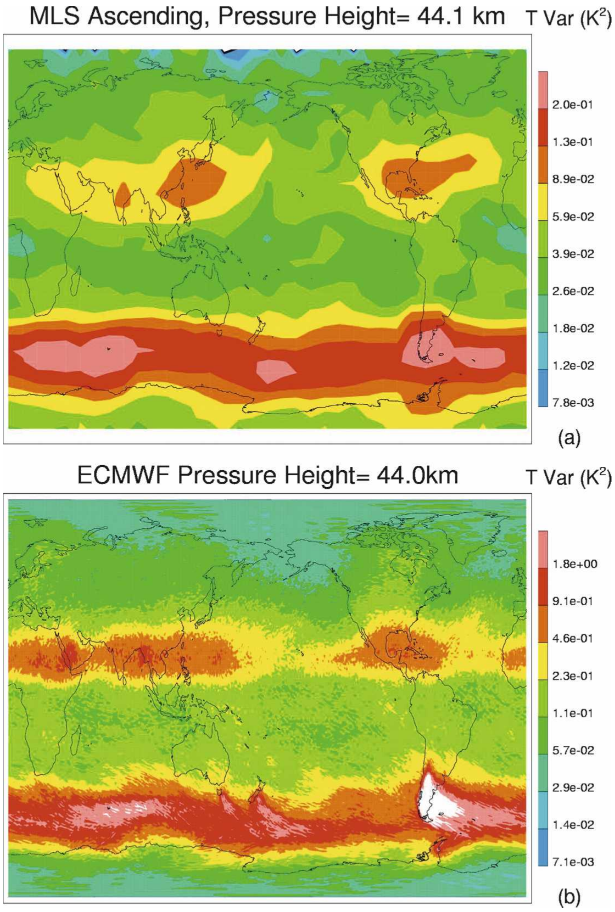

FIG. 12. Map of monthly-mean GW temperature variance at ~44-km pressure altitude from (a) the *Aura* MLS GW variance from channels 11/15 and (b) ECMWF IFS T_L799L91 analyses for every day of August 2006. As in Figs. 10–11, temperature perturbations in the ECMWF IFS analyses were truncated to exclude horizontal wavelengths >~300 km before the variance was computed, but no vertical filter was applied.

variances from the T_L799L91 analyses are enhanced in two distinct latitude bands in which strong background winds increase the probability of MLS-resolvable GW vertical wavelengths in the stratosphere. The longitudinal modulation of the GW variances in these latitude bands suggests a nonuniform distribution of GW sources. For example, in the high-latitude southern band, mountain waves from the southern Andes are the most prominent feature in Fig. 12b, as they are in the GW variances from *Aura* MLS (Fig. 12a) and those derived from other satellite instruments. The orographic GWs from the southern Andes propagate with large amplitudes thousands of kilometers downstream, as was observed from satellite and modeled by Preusse et al. (2002).

A band of enhanced IFS variance also occurs in the northern subtropics in Fig. 12b, with variance peaks occurring over southern United States/Mexico and Southeast Asia, features also seen in the *Aura* MLS GW variances in Fig. 12a (see also Fig. 7). The subtropical GW variance band from ECMWF IFS is slightly narrower latitudinally and displaced equatorward of the *Aura* MLS band. These differences may be related to slightly different GW vertical and horizontal wavelength sensitivities in each dataset or to the IFS's convectively generated tropical GW spectrum, whose properties in global models prove highly sensitive to the way in which deep cumulus convection is parameterized (e.g., Horinouchi et al. 2003).

The overall similarities in Fig. 12 highlight the global GW-resolving capabilities of both high-resolution satellite remote sensors like the *Aura* MLS and high-resolution global models like the T_L799L91 ECMWF IFS. Such comparisons illustrate the potential benefits of these *Aura* MLS GW data for validating the stratospheric GWs explicitly simulated and parameterized in global models.

6. Summary and future work

In this investigation, we have characterized the sensitivity of *Aura* MLS saturated 118-GHz radiances to stratospheric GWs of different wavelengths and have used these insights to interpret the GW-induced radiance perturbations that are located at the bottom of each normal limb scan. We have shown that small-scale perturbations in these saturated radiances are produced by horizontally varying GW-induced temperature oscillations within a broad vertical atmospheric layer whose mean pressure altitude varies from ~21.7 km for channels 1 and 25 to ~51 km for channels 12 and 14. Vertical and along-track smearing by the MLS weighting functions (WFs) limit the instrument's sensitivity to GWs. Forward modeling shows that the MLS has greatest sensitivity to high-frequency GWs with short horizontal and long vertical wavelengths that propagate toward the instrument. This leads to anisotropy between GW variances measured on ascending and descending orbits, from which one can infer preferred northward or southward GW propagation components. The much narrower vertical field of view (FOV) and smaller channel noise of *Aura* MLS yield much improved sensitivity to GWs of all scales compared to the *UARS* MLS, particularly to GWs of shorter vertical wavelength. The *Aura* MLS also provides variance data in the altitude region 21–28 km that was not covered by the *UARS* MLS thermal radiance channels. By extending the analysis to MLS 118-GHz channels located farther from and closer to the O_2 line center, it will be possible in future studies to observe GW variances at pressure altitudes down to ~15 km and up to ~95 km, respectively.

We used these capabilities to study GWs by first forming variances using the 40 saturated radiances located at the bottom of each limb scan, which yielded global data at twelve independent altitudes between 21 and 51 km. *Aura* MLS data acquired between late 2004 and mid-2007 were processed in this way and analyzed as a function of time, altitude, and geographical location. The main findings were as follows:

1) The MLS variances at 21–28-km altitude are enhanced at the tropics. The similar distribution in GW activity has been observed by high–vertical resolution satellite limb sounders and ground-based profilers, but in the MLS case the variances are contributed mostly from waves with long (>5 km) vertical and short (<300 km) horizontal wavelengths.
2) These tropical GW variances show significant variations with QBO phase that agree with long-term tropical GW variances measured by sondes. The enhanced tropical MLS GW variance at 21.7 km is split into twin-peaked subtropical bands during the westerly (eastward) QBO wind phase and then reverts to a single strong equatorial peak during the easterly (westward) QBO phase.
3) Antarctic GW variances at 21–25-km altitude peak during October–November, whereas at higher altitudes they peak in midwinter. These findings agree with radiosonde and GPS data from this region.
4) The variances in the upper stratosphere are similar in morphology to those from the *UARS* MLS, with seasonal and latitudinal enhancements correlating strongly with related increases in background wind speeds that refract GWs to the long vertical wavelength scales needed for MLS to resolve them (e.g., Alexander 1998).
5) Longitudinal asymmetries reveal sources, such as strong orographic GW activity over the Antarctic Peninsula, New Zealand, Alaska, Scandinavia, Greenland, and the Andes, Alps, and Appalachian and Rocky Mountains during winter. Localized regions of enhanced tropical and subtropical variance correlate well with enhanced convection (diagnosed using the MLS cloud ice product) over the Maritime Continent, South America, southern Asia, and the southeastern United States. Preferred meridional components of propagation for GWs in all these regions were inferred from the differences in variance measured on ascending and descending orbits.

We briefly compared the GW variances observed by the MLS in August 2006 to the explicitly resolved GW temperature oscillations in the $\mathrm{T_L}$799L91 ECMWF IFS analyses at a pressure altitude of ~44 km. The monthly-mean variance maps showed many similarities, including latitudinal bands of enhanced variance in regions of high background wind speed and over regions of enhanced orographic and convective GW forcing. These comparisons highlight the potentially valuable role that *Aura* MLS GW observations can play in validating both the explicitly simulated GWs in very high-resolution models and those parameterized in low-resolution climate–chemistry models. More detailed model–observation comparisons require forward modeling of 3D model temperature fields using the *Aura* MLS 3D WFs and in-orbit sampling patterns (e.g., Jiang et al. 2004a; Eckermann and Wu 2006; Eckermann et al. 2006b), which we will explore in future work.

Future studies will also analyze GW perturbations in other MLS radiance channels that have better vertical resolution in the lower stratosphere. For example, MLS 240- and 640-GHz radiances have vertical FOVs of 3.2 and 1.4 km, respectively, at the tangent point, but the measurement noise at these frequencies is, respectively, 1.3 and 3.5 times larger than the 118-GHz measurements. Despite these larger noise variances, the improved sensitivity to the 2–4-km vertical wavelength GWs that dominate lower stratospheric GW variance (Allen and Vincent 1995) may well yield significantly higher signal-to-noise ratios (SNRs) for GW variances at these altitudes. In addition, we can increase the SNR by employing a longer horizontal truncation length for the GW variance calculation (e.g., Jiang et al. 2002). This is potentially attractive for resolving the low-frequency GWs with long horizontal but short vertical wavelengths that dominate equatorial variances (Sato and Dunkerton 1997; Vincent and Alexander 2000; Alexander et al. 2002; Ern et al. 2004; Wang et al. 2005). A long truncation length can be obtained by analyzing MLS radiances from adjacent limb scans that are separated by ~165 km. By binning 3–4 adjacent scans of MLS radiances, we will be able to increase the cutoff horizontal wavelengths to 500–600 km. For all the GW studies extended to long horizontal wavelengths, however, we need to be careful not to alias in planetary waves (e.g., Kelvin or mixed Rossby–gravity waves). The inability to distinguish GWs from planetary waves, which often have vertical wavelengths as short as 3–4 km, has been an issue with GW observations from radiosondes, rocketsondes, and other satellite limb techniques (e.g., Eckermann 1995).

Acknowledgments. This work was supported by NASA program NNH04ZYS004N (“Measurements, Modeling, and Analyses in Support of *Aura* and Other Satellite Observations of the Earth’s Atmosphere”).

DLW's research was performed at the Jet Propulsion Laboratory (JPL), California Institute of Technology under contract with the National Aeronautics and Space Administration (NASA) and supported by the NASA *Aura* project. SDE acknowledges additional support from NASA's Geospace Sciences SR&T Program. We thank the UK Met Office for providing stratospheric wind analyses and the ECMWF for providing T_L799L91 IFS analysis data. Assistance from Dr. Evan Fishbein in accessing the ECMWF data is also acknowledged. Finally, we thank the JPL MLS team for successful instrument development, operation, and data processing, and three anonymous reviewers for valuable comments on the original manuscript.

REFERENCES

Alexander, M. J., 1998: Interpretations of observed climatological patterns in stratospheric gravity wave variance. *J. Geophys. Res.,* **103,** 8627–8640.

——, and C. Barnet, 2007: Using satellite observations to constrain parameterizations of gravity wave effects for global models. *J. Atmos. Sci.,* **64,** 1652–1665.

——, and H. Teitelbaum, 2007: Analysis and observation of a large-amplitude mountain wave event over the Antarctic Peninsula. *J. Geophys. Res.,* **112,** D21103, doi:10.1029/2006JD008368.

——, T. Tsuda, and R. A. Vincent, 2002: Latitudinal variations observed in gravity waves with short vertical wavelengths. *J. Atmos. Sci.,* **59,** 1394–1404.

——, P. T. May, and J. H. Beres, 2004: Gravity waves generated by convection in the Darwin area during the Darwin Area Wave Experiment. *J. Geophys. Res.,* **109,** D20S04, doi:10.1029/2004JD004729.

Allen, S. J., and R. A. Vincent, 1995: Gravity wave activity in the lower atmosphere: Seasonal and latitudinal variations. *J. Geophys. Res.,* **100,** 1327–1350.

Bacmeister, J. T., S. D. Eckermann, P. A. Newman, L. Lait, K. R. Chan, M. Loewenstein, M. H. Proffitt, and B. L. Gary, 1996: Stratospheric horizontal wavenumber spectra of winds, potential temperature, and atmospheric tracers observed by high-altitude aircraft. *J. Geophys. Res.,* **101,** 9441–9470.

Baldwin, M. P., and Coauthors, 2001: The quasi-biennial oscillation. *Rev. Geophys.,* **39** (2), 179–229.

Baumgaertner, A. J. G., and A. J. McDonald, 2007: A gravity wave climatology for Antarctica compiled from Challenging Minisatellite Payload/Global Positioning System (CHAMP/GPS) radio occultations. *J. Geophys. Res.,* **112,** D05103, doi:10.1029/2006JD007504.

Chane-Ming, F., G. Roff, L. Robert, and J. Leveau, 2002: Gravity wave characteristics over Tromelin Island during the passage of cyclone Hudah. *Geophys. Res. Lett.,* **29,** 1094, doi:10.1029/2001GL013286.

Cofield, R. E., and P. C. Stek, 2006: Design and field-of-view calibration of 114–660-GHz optics of the Earth Observing System Microwave Limb Sounder. *IEEE Trans. Geosci. Remote Sens.,* **44,** 1166–1181.

De la Torre, A., T. Schmidt, and J. Wickert, 2006: A global analysis of wave potential energy in the lower stratosphere derived from 5 years of GPS radio occultation data with CHAMP. *Geophys. Res. Lett.,* **33,** L24809, doi:10.1029/2006GL027696.

Eckermann, S. D., 1995: On the observed morphology of gravity-wave and equatorial-wave variance in the stratosphere. *J. Atmos. Terr. Phys.,* **57,** 105–134.

——, and P. Preusse, 1999: Global measurements of stratospheric mountain waves from space. *Science,* **286,** 1534–1537.

——, and D. L. Wu, 2006: Imaging gravity waves in lower stratospheric AMSU-A radiances. Part 1: Simple forward model. *Atmos. Chem. Phys.,* **6,** 3325–3341.

——, I. Hirota, and W. K. Hocking, 1995: Gravity-wave and equatorial-wave morphology of the stratosphere derived from long-term rocket soundings. *Quart. J. Roy. Meteor. Soc.,* **121,** 149–186.

——, A. Dörnbrack, S. B. Vosper, H. Flentje, M. J. Mahoney, T. P. Bui, and K. S. Carslaw, 2006a: Mountain wave–induced polar stratospheric cloud forecasts for aircraft science flights during SOLVE/THESEO 2000. *Wea. Forecasting,* **21,** 42–68.

——, and Coauthors, 2006b: Imaging gravity waves in lower stratospheric AMSU-A radiances. Part 2: Validation case study. *Atmos. Chem. Phys.,* **6,** 3343–3362.

Ern, M., P. Preusse, M. J. Alexander, and C. D. Warner, 2004: Absolute values of gravity wave momentum flux derived from satellite data. *J. Geophys. Res.,* **109,** D20103, doi:10.1029/2004JD004752.

Fetzer, E. J., and J. C. Gille, 1994: Gravity wave variance in LIMS temperatures. Part I: Variability and comparison with background winds. *J. Atmos. Sci.,* **51,** 2461–2483.

Fritts, D. C., and M. J. Alexander, 2003: Gravity wave dynamics and effects in the middle atmosphere. *Rev. Geophys.,* **41,** 1003, doi:10.1029/2001RG000106.

——, S. L. Vadas, K. Wan, and J. A. Werne, 2006: Mean and variable forcing of the middle atmosphere by gravity waves. *J. Atmos. Solar-Terr. Phys.,* **68,** 247–265.

Guest, F. M., M. J. Reeder, C. J. Marks, and D. J. Karoly, 2000: Inertia–gravity waves observed in the lower stratosphere over Macquarie Island. *J. Atmos. Sci.,* **57,** 737–752.

Hertzog, A., C. Souprayen, and A. Hauchecorne, 2001: Observation and backward trajectory of an inertio-gravity wave in the lower stratosphere. *Ann. Geophys.,* **19,** 1141–1155.

——, F. Vial, A. Dörnbrack, S. D. Eckermann, B. M. Knudsen, and J.-P. Pommereau, 2002: In situ observations of gravity waves and comparisons with numerical simulations during the SOLVE/THESEO 2000 campaign. *J. Geophys. Res.,* **107,** 8292, doi:10.1029/2001JD001025.

Horinouchi, T., and Coauthors, 2003: Tropical cumulus convection and upward-propagating waves in middle-atmospheric GCMs. *J. Atmos. Sci.,* **60,** 2765–2782.

Jarnot, R. F., R. E. Cofield, J. W. Waters, D. A. Flower, and G. E. Peckham, 1996: Calibration of the Microwave Limb Sounder on the Upper Atmosphere Research Satellite. *J. Geophys. Res.,* **101,** 9957–9982.

Jiang, J. H., and D. L. Wu, 2001: UARS MLS observations of gravity waves associated with the Arctic winter stratospheric vortex. *Geophys. Res. Lett.,* **28,** 527–530.

——, ——, and S. D. Eckermann, 2002: Upper Atmosphere Research Satellite (UARS) MLS observation of mountain waves over the Andes. *J. Geophys. Res.,* **107,** 8273, doi:10.1029/2002JD002091.

——, S. D. Eckermann, D. L. Wu, and J. Ma, 2004a: A search for mountain waves in MLS stratospheric limb radiances from the winter Northern Hemisphere: Data analysis and global mountain wave modeling. *J. Geophys. Res.,* **109,** D03107, doi:10.1029/2003JD003974.

——, B. Wang, K. Goya, K. Hocke, S. D. Eckermann, J. Ma, D. L. Wu, and W. G. Read, 2004b: Geographical distribution and interseasonal variability of tropical deep convection: UARS MLS observations and analyses. *J. Geophys. Res.,* **109,** D03111, doi:10.1029/2003JD003756.

——, S. D. Eckermann, D. L. Wu, K. Hocke, B. Wang, J. Ma, and Y. Zhang, 2005: Seasonal variation of gravity wave sources from satellite observation. *Adv. Space Res.,* **35,** 1925–1932.

——, ——, D. L. Wu, and D.-Y. Wang, 2006: Interannual variation of gravity waves in the Arctic and Antarctic winter middle atmosphere. *Adv. Space Res.,* **38,** 2418–2423.

Kim, S.-Y., H.-Y. Chun, and J.-J. Baik, 2005: A numerical study of gravity waves induced by convection associated with Typhoon Rusa. *Geophys. Res. Lett.,* **32,** L24816, doi:10.1029/2005GL024662.

Kim, Y.-J., S. D. Eckermann, and H.-Y. Chun, 2003: An overview of the past, present, and future of gravity-wave drag parametrization for numerical climate and weather prediction models. *Atmos.–Ocean,* **41,** 65–98.

Koshyk, J. N., and K. Hamilton, 2001: The horizontal kinetic energy spectrum and spectral budget simulated by a high-resolution troposphere–stratosphere–mesosphere GCM. *J. Atmos. Sci.,* **58,** 329–348.

Krebsbach, M., and P. Preusse, 2007: Spectral analysis of gravity wave activity in SABER temperature data. *Geophys. Res. Lett.,* **34,** L03814, doi:10.1029/2006GL028040.

McLandress, C., 1998: On the importance of gravity waves in the middle atmosphere and their parameterization in general circulation models. *J. Atmos. Solar-Terr. Phys.,* **60,** 1357–1383.

——, and J. F. Scinocca, 2005: The GCM response to current parameterizations of nonorographic gravity wave drag. *J. Atmos. Sci.,* **62,** 2394–2413.

——, M. J. Alexander, and D. L. Wu, 2000: Microwave limb sounder observations of gravity waves in the stratosphere: A climatology and interpretation. *J. Geophys. Res.,* **105,** 11 947–11 967.

O'Sullivan, D., and T. J. Dunkerton, 1995: Generation of inertia–gravity waves in a simulated life cycle of baroclinic instability. *J. Atmos. Sci.,* **52,** 3695–3716.

Pfenninger, M., A. Z. Liu, G. C. Papen, and C. S. Gardner, 1999: Gravity wave characteristics in the lower atmosphere at the South Pole. *J. Geophys. Res.,* **104,** 5963–5984.

Plougonven, R., and H. Teitelbaum, 2003: Comparison of a large-scale inertia–gravity wave as seen in the ECMWF analyses and from radiosondes. *Geophys. Res. Lett.,* **30,** 1954, doi:10.1029/2003GL017716.

Preusse, P., S. D. Eckermann, and D. Offermann, 2000: Comparison of global distributions of zonal-mean gravity wave variance inferred from different satellite instruments. *Geophys. Res. Lett.,* **27,** 3877–3880.

——, A. Dörnbrack, S. D. Eckermann, M. Riese, B. Schaeler, J. T. Bacmeister, D. Broutman, and K. U. Grossmann, 2002: Space-based measurements of stratospheric mountain waves by CRISTA. 1. Sensitivity, analysis method, and a case study. *J. Geophys. Res.,* **107,** 8178, doi:10.1029/2001JD000699.

——, and Coauthors, 2006: Tropopause to mesopause gravity waves in August: Measurement and modeling. *J. Atmos. Solar-Terr. Phys.,* **68,** 1730–1751.

Randel, W. J., and F. Wu, 2005: Kelvin wave variability near the equatorial tropopause observed in GPS radio occultation measurements. *J. Geophys. Res.,* **110,** D03102, doi:10.1029/2004JD005006.

Ratnam, M. V., G. Tetzlaff, and C. Jacobi, 2004: Global and seasonal variations of stratospheric gravity wave activity deduced from the *CHAMP*/GPS satellite. *J. Atmos. Sci.,* **61,** 1610–1620.

Read, W. G., Z. Shippony, M. J. Schwartz, N. J. Livesey, and W. Van Snyder, 2006: The clear-sky unpolarized forward model for the EOS *Aura* Microwave Limb Sounder (MLS). *IEEE Trans. Geosci. Remote Sens.,* **44,** 1367–1379.

Sato, K., 1993: Small-scale wind disturbances observed by the MU radar during the passage of Typhoon Kelly. *J. Atmos. Sci.,* **50,** 518–537.

——, and T. J. Dunkerton, 1997: Estimates of momentum flux associated with equatorial Kelvin and gravity waves. *J. Geophys. Res.,* **102,** 26 247–26 261.

Siskind, D. E., S. D. Eckermann, L. Coy, J. P. McCormack, and C. E. Randall, 2007: On recent interannual variability of the Arctic winter mesosphere: Implications for tracer descent. *Geophys. Res. Lett.,* **34,** L09806, doi:10.1029/2007GL029293.

Tsuda, T., T. E. VanZandt, M. Mizumoto, S. Kato, and S. Fukao, 1991: Spectral analysis of temperature and Brunt–Väisälä frequency fluctuations observed by radiosondes. *J. Geophys. Res.,* **96,** 17 265–17 278.

——, M. Nishida, C. Rocken, and R. H. Ware, 2000: A global morphology of gravity wave activity in the stratosphere revealed by the GPS occultation data (GPS/MET). *J. Geophys. Res.,* **105,** 7257–7273.

——, M. V. Ratnam, P. T. May, M. J. Alexander, R. A. Vincent, and A. MacKinnon, 2004: Characteristics of gravity waves with short vertical wavelengths observed with radiosonde and GPS occultation during DAWEX (Darwin Area Wave Experiment). *J. Geophys. Res.,* **109,** D20S03, doi:10.1029/2004JD004946.

Vincent, R. A., and M. J. Alexander, 2000: Gravity waves in the tropical lower stratosphere: An observational study of seasonal and interannual variability. *J. Geophys. Res.,* **105,** 17 971–17 982.

Wada, K., T. Nitta, and K. Sato, 1999: Equatorial inertia-gravity waves in the lower stratosphere revealed by TOGA-COARE IOP data. *J. Meteor. Soc. Japan,* **77,** 721–736.

Wang, L., 2003: Gravity wave analysis of four years of high vertical resolution U.S. radiosonde data. Ph.D. thesis, Stony Brook University, 227 pp.

——, and M. A. Geller, 2003: Morphology of gravity-wave energy as observed from 4 years (1998–2001) of high vertical resolution U.S. radiosonde data. *J. Geophys. Res.,* **108,** 4489, doi:10.1029/2002JD002786.

——, ——, and M. J. Alexander, 2005: Spatial and temporal variations of gravity wave parameters. Part I: Intrinsic frequency, wavelength, and vertical propagation direction. *J. Atmos. Sci.,* **62,** 125–142.

Waters, J. W., and Coauthors, 2006: The Earth Observing System Microwave Limb Sounder (EOS MLS) on the *Aura* satellite. *IEEE Trans. Geosci. Remote Sens.,* **44,** 1075–1092.

Whiteway, J. A., 1999: Enhanced and inhibited gravity wave spectra. *J. Atmos. Sci.,* **56,** 1344–1352.

——, and A. I. Carswell, 1994: Rayleigh lidar observations of thermal structure and gravity wave activity in the high Arctic during a stratospheric warming. *J. Atmos. Sci.,* **51,** 3122–3136.

Wu, D. L., 2001: Horizontal wavenumber spectra of MLS radiance fluctuations. *J. Atmos. Solar-Terr. Phys.,* **63,** 1465–1477.

——, 2004: Mesoscale gravity wave variances from AMSU-A radiances. *Geophys. Res. Lett.,* **31,** L12114, doi:10.1029/2004GL019562.

——, 2006: Small-scale fluctuations and scintillations in high-resolution GPS/CHAMP SNR and phase data. *J. Atmos. Solar-Terr. Phys.,* **68,** 999–1017.

——, and J. W. Waters, 1996: Satellite observations of atmospheric variances: A possible indication of gravity waves. *Geophys. Res. Lett.,* **23,** 3631–3634.

——, and ——, 1997: Observations of gravity waves with the UARS Microwave Limb Sounder. *Gravity Wave Processes and Their Parameterization in Global Climate Models,* K. Hamilton, Ed., NATO ASI Series, Vol. 50, Springer-Verlag, 103–120.

——, and F. Zhang, 2004: A study of mesoscale gravity waves over the North Atlantic with satellite observations and a mesoscale model. *J. Geophys. Res.,* **109,** D22104, doi:10.1029/2004JD005090.

——, P. Preusse, S. D. Eckermann, J. H. Jiang, M. de la Torre Juarez, L. Coy, and D. Y. Wang, 2006a: Remote sounding of atmospheric gravity waves with satellite limb and nadir techniques. *Adv. Space Res.,* **37,** 2269–2277.

——, J. H. Jiang, and C. Davis, 2006b: EOS MLS cloud ice measurements and cloudy-sky radiative transfer model. *IEEE Trans. Geosci. Remote Sens.,* **44,** 1156–1165.

Yoshiki, M., and K. Sato, 2000: A statistical study of gravity waves in the polar regions based on operational radiosonde data. *J. Geophys. Res.,* **105,** 17 995–18 011.

——, N. Kizu, and K. Sato, 2004: Energy enhancements of gravity waves in the Antarctic lower stratosphere associated with variations in the polar vortex and tropospheric disturbances. *J. Geophys. Res.,* **109,** D23104, doi:10.1029/2004JD004870.